The viscosities of partially molten materials undergoing diffusion creep

John F. Rudge

Bullard Laboratories, Department of Earth Sciences, University of Cambridge, Madingley Road, Cambridge, CB3 0EZ, UK.

Key Points:

- Calculations of the effective shear and bulk viscosities of texturally equilibrated partially molten materials are presented.
- Nabarro-Herring creep calculations show a logarithmic singularity in the bulk viscosity at small porosities.
- Coble creep calculations show a drop in the shear viscosity at the onset of melting, but a more modest drop than previously reported.

Corresponding author: John F. Rudge, jfr23@cam.ac.uk

Abstract

Partially molten materials resist shearing and compaction. This resistance is described by a fourth-rank effective viscosity tensor. When the tensor is isotropic, two scalars determine the resistance: an effective shear and an effective bulk viscosity. Here, calculations are presented of the effective viscosity tensor during diffusion creep for a 2D tiling of hexagonal unit cells and a 3D tessellation of tetrakaidecahedrons (truncated octahedrons). The geometry of the melt is determined by assuming textural equilibrium. The viscosity tensor for the 2D tiling is isotropic, but that for the 3D tessellation is anisotropic. Two parameters control the effect of melt on the viscosity tensor: the porosity and the dihedral angle. Calculations for both Nabarro-Herring (volume diffusion) and Coble (surface diffusion) creep are presented. For Nabarro-Herring creep the bulk viscosity becomes singular as the porosity vanishes. This singularity is logarithmic, a weaker singularity than typically assumed in geodynamic models. The presence of a small amount of melt (0.1% porosity) causes the effective shear viscosity to approximately halve. For Coble creep, previous modelling work has argued that a very small amount of melt may lead to a substantial, factor of 5, drop in the shear viscosity. Here, a much smaller, factor of 1.4, drop is obtained for tetrakaidecahedrons. Owing to a Cauchy relation symmetry, the Coble creep bulk viscosity is a constant multiple of the shear viscosity when melt is present.

1 Introduction

Dynamical models are often highly dependent on assumptions about the rheology of the material being deformed. In many situations in the Earth Sciences, this rheology is poorly known, and this is particularly true of the polycrystalline rocks in the partially molten regions of the Earth's mantle. There are two main approaches to making progress towards a better understanding of rheology: One approach is to perform deformation experiments on materials in the laboratory, and parametrise the results of these experiments into empirical laws (e.g. Mei, Bai, Hiraga, and Kohlstedt (2002)). A second approach is to produce models of the microscale physics and upscale these models to produce rheological laws suitable for use at larger scales (e.g. Cooper & Kohlstedt, 1984; Takei & Holtzman, 2009a). This study follows the second approach.

One of the remarkable features of the Earth's mantle is its ability to flow on long time scales, despite being solid for the most part. This flow is only possible because the solid is fairly close to its melting temperature, which enables creep by the diffusive trans-

port of matter in the solid phase. Diffusion creep comes in two main types: Nabarro-Herring creep (Herring, 1950; Nabarro, 1948), where diffusion takes place through the bodies of grains, and Coble creep (Coble, 1963), where diffusion takes place along the boundaries between grains. Due to the different activation enthalpies and grain-size dependencies of the two diffusion mechanisms, Nabarro-Herring creep dominates for large grains and high temperatures; Coble creep for small grains and low temperatures.

A pure solid material resists shear, and that resistance to shear is characterised by a shear viscosity, which for diffusion creep can be calculated from simple mathematical models of the diffusive transport of matter (Coble, 1963; Herring, 1950; Lifshitz, 1963). A partially molten material allows an additional mode of deformation, compaction, whereby grains are packed closer together and melt is expelled under an isotropic stress. The resistance to this kind of deformation can be described in terms of an effective bulk viscosity (McKenzie, 1984), which can also be determined using microscale models of diffusion (Arzt, Ashby, & Easterling, 1983; Cocks, 1996; Cocks & Searle, 1990; Takei & Holtzman, 2009a).

In partially molten materials undergoing diffusion creep, the presence of melt causes a reduction in the effective shear viscosity of the material compared to the melt-free situation. One reason for this is that diffusion in the melt phase is typically much faster than in the solid phase (Cooper & Kohlstedt, 1984; Takei & Holtzman, 2009a). Since the rate of diffusion creep is dependent on the rate at which material can be transported from one part of a grain to another, the presence of fast melt pathways speeds up the overall rate of creep for a given stress. How large this effect is depends crucially on the geometry of the melt at the grain scale. The simplest model of melt geometry at the grain scale is that of textural equilibrium, a state which minimises surface energy. Calculations of such melt geometries have recently been presented for a tessellation of tetrakaidecahedral unit cells (Rudge, 2018). The aim of this manuscript is to explore the effect of melt on creep viscosities using these geometries.

This work can be seen as a direct extension of the work by Takei and Holtzman (2009a). That study presented a detailed account of the effect of melt on viscosity during Coble creep, but made a series of approximations to the geometry (spherical grains with circular contact patches) to allow analytical solutions to be obtained for the relevant diffusion problems. Here, the diffusion problems are solved numerically by the fi-

nite element method using the full geometries. Moreover, in this study, both Nabarro-Herring creep and Coble creep are considered.

The manuscript is organised as follows. The next section presents an overview of the governing equations of diffusion creep, both for Nabarro-Herring creep and Coble creep. Section 3 gives results of the creep calculations for the textural equilibrium geometries. To build insight, for each type of diffusion creep the case of a 2D hexagonal array of grains is considered first before examining the 3D case. Discussion and conclusions sections follow that compare these results to those in the wider literature. Detailed mathematical derivations are given in the appendices.

2 Governing equations

The basic governing equations of diffusion creep are well-established and can be found in many previous studies (e.g. Cocks (1996); Cocks and Searle (1990); Herring (1950); Lifshitz (1963); Nabarro (1948); Takei and Holtzman (2009a)). These equations establish the relationship between the macroscale stress and strain tensors, which can be written in terms of a fourth-rank effective viscosity tensor. The presentation of the equations given below largely follows Lifshitz (1963) in expressing all relationships in tensor form, and follows Cocks and Searle (1990) and Takei and Holtzman (2009a) in its treatment of the melt phase.

2.1 Nabarro-Herring (volume diffusion) creep

Let the concentration of vacancies (number of vacancies per unit volume) in the solid grain be c. Fick's law describes the motion of vacancies within the grain, with flux

$$\mathbf{j}_\mathrm{v} = -D_\mathrm{v}\nabla c, \tag{1}$$

where D_v is the diffusivity of vacancies. There is a corresponding flux $\mathbf{j} = -\mathbf{j}_\mathrm{v}$ of atoms. Conservation of vacancies within the grain ($\nabla\cdot\mathbf{j}_\mathrm{v} = 0$, assuming a quasi-static approximation) yields Laplace's equation for the concentration of vacancies

$$\nabla^2 c = 0. \tag{2}$$

The grain changes shape because of the flux of vacancies to the boundaries of the grain, which are assumed to act as perfect sources and sinks for vacancies. The shape change is described by the plating rate $\dot{r}$, which quantifies the rate at which a boundary grows,

and is given by

$$\dot{r} = -\Omega \mathbf{j}_{\mathrm{v}} \cdot \mathbf{n} \tag{3}$$

where Ω is the atomic volume, and $\mathbf{n}$ is the normal outward to the grain. For the regular tessellations of identical grains considered here, we will assume grain boundaries are perpendicular to lines connecting neighbouring grain centres. Addition or loss of material at the grain boundaries leads to a change of shape of the grain, which manifests as a macroscopic strain rate $\dot{\underline{\underline{\boldsymbol{e}}}}$. To maintain compatability between grains during deformation, the assumption will be made that the polyhedral grain remains polyhedral (all grain boundaries remain flat). Thus the plating rate $\dot{r}$ will be a constant on each planar face of the grain (Cocks & Searle, 1990). Coordinates are chosen such that the centre of mass of the grain is the origin, and it will be assumed this point is fixed. The plating rate $\dot{r}$ on the planar grain boundaries can then be related to the strain rate tensor $\dot{\underline{\underline{\boldsymbol{e}}}}$ by

$$\mathbf{n} \cdot \dot{\underline{\underline{\boldsymbol{e}}}} \cdot \mathbf{n} = \frac{\dot{r}}{\mathbf{x} \cdot \mathbf{n}}, \tag{4}$$

where $\mathbf{x}\cdot\mathbf{n}$ is the perpendicular distance of the plane from the centre of the grain, and $\mathbf{x}$ is the position vector of a point on the plane. Gradients in vacancy concentration are created because the grain is under stress, and this changes the equilibrium concentration of vacancies at the grain boundaries, which depends on the normal stress on those boundaries. Unlike the plating rate, the normal stress varies over each grain boundary. A linearised relationship between the concentration of vacancies and the normal stress is given by (Herring, 1950)

$$c = c_0 \left(1 + \frac{\Omega}{kT} \mathbf{n} \cdot \underline{\underline{\boldsymbol{\sigma}}}^s \cdot \mathbf{n}\right) \text{ on } S, \tag{5}$$

where S is the surface of the grain, c_0 is the equilibrium concentration of vacancies, k is the Boltzmann constant, and T is temperature. For a partially molten system, the surface of the grain can be divided into two types: a section of grain–grain contact (S_{ss}) and a section of grain–liquid contact (S_{sl}). On areas of contact with the liquid it will be assumed that

$$\underline{\underline{\boldsymbol{\sigma}}}^s \cdot \mathbf{n} = -P^l \mathbf{n} \text{ on } S_{\mathrm{sl}}, \tag{6}$$

where P^l is the liquid pressure (surface tension across the solid–liquid interface is neglected). Implicit in this boundary condition is an assumption that all the melt pores are connected and at the same pressure. Conservation of momentum inside the grain is

$$\nabla \cdot \underline{\underline{\boldsymbol{\sigma}}}^s = \mathbf{0}. \tag{7}$$

It will be assumed that grains can slide freely at grain-boundaries (Lifshitz, 1963; Raj & Ashby, 1971), and thus the corresponding shear stresses are relaxed,

$$\mathbf{t} \cdot \underline{\underline{\boldsymbol{\sigma}}}^s \cdot \mathbf{n} = 0 \text{ on } S_{ss}, \tag{8}$$

where $\mathbf{t}$ is a vector tangential to the boundary plane. The main quantity of interest is the mean stress inside the grain, defined by

$$\overline{\underline{\boldsymbol{\sigma}}}^s \equiv \frac{1}{V_\mathrm{s}} \int \underline{\underline{\boldsymbol{\sigma}}}^s \, \mathrm{d}V, \tag{9}$$

where V_s is the volume of the grain. The ultimate aim of the creep calculations is to relate this mean stress $\overline{\underline{\boldsymbol{\sigma}}}^s$ to the macroscopic strain rate $\underline{\dot{\boldsymbol{e}}}$. This can be done without explicitly solving for the stress inside the grain, because the mean stress inside the grain can be related to the boundary tractions $\underline{\underline{\boldsymbol{\sigma}}}^s \cdot \mathbf{n}$ by

$$\int \underline{\underline{\boldsymbol{\sigma}}}^s \, \mathrm{d}V = \int \underline{\underline{\boldsymbol{\sigma}}}^s + \left(\nabla \cdot \underline{\underline{\boldsymbol{\sigma}}}^s\right) \mathbf{x} \, \mathrm{d}V = \int \nabla \cdot \left(\underline{\underline{\boldsymbol{\sigma}}}^s \mathbf{x}\right) \, \mathrm{d}V = \int \mathbf{x} \, \underline{\underline{\boldsymbol{\sigma}}}^s \cdot \mathbf{n} \, \mathrm{d}S \tag{10}$$

where the first equality exploits the conservation of momentum (7), and the final equality exploits the divergence theorem and the symmetry of the stress tensor. Furthermore, because the boundaries are assumed to be free-slipping (8), the boundary tractions are purely normal, and can be written $\underline{\underline{\boldsymbol{\sigma}}}^s \cdot \mathbf{n} = (\mathbf{n} \cdot \underline{\underline{\boldsymbol{\sigma}}}^s \cdot \mathbf{n})\mathbf{n}$. Hence,

$$\overline{\underline{\boldsymbol{\sigma}}}^s = \frac{1}{V_\mathrm{s}} \int (\mathbf{n} \cdot \underline{\underline{\boldsymbol{\sigma}}}^s \cdot \mathbf{n}) \, \mathbf{x} \, \mathbf{n} \, \mathrm{d}S \tag{11}$$

In turn, $\mathbf{n} \cdot \underline{\underline{\boldsymbol{\sigma}}}^s \cdot \mathbf{n}$ can be related directly to the concentration of vacancies through (5).

2.1.1 Scaling

The equations above can be simplified by scaling to produce dimensionless governing equations. All lengths can be scaled on a characteristic length scale d (a measure of grain size). It is useful to introduce the self-diffusion coefficient $D = D_v c_0 \Omega$, and scale all times with the diffusive timescale $\tau = d^2/D$. A natural scale for stresses (and thus pressure) is given from (5) as $P_0 = kT/\Omega$. It follows that a natural scale for viscosities is $P_0 \tau = kTd^2/D\Omega$, which is the classic scaling of Nabarro-Herring creep, with viscosities proportional to the square of grain size. For the concentration of vacancies it is useful to introduce a scaled variable as

$$c' = \frac{c}{c_0} - 1 + P^{l\prime} \tag{12}$$

where $P^{l\prime} = P^l/P_0$ is the scaled liquid pressure. The dimensionless governing equations are then

$$\nabla^2 c = 0 \text{ in } V_\mathrm{s}, \tag{13}$$

$$c = 0 \text{ on } S_\mathrm{sl}, \tag{14}$$

$$\frac{\partial c}{\partial n} = \left(\mathbf{n}\cdot\underline{\underline{\dot{\boldsymbol{e}}}}\cdot\mathbf{n}\right)\mathbf{x}\cdot\mathbf{n} \text{ on } S_\mathrm{ss}, \tag{15}$$

$$\underline{\underline{\overline{\boldsymbol{\sigma}}}}^s = -P^l\underline{\underline{\boldsymbol{I}}} + \frac{1}{V_\mathrm{s}}\int c\,\mathbf{x}\,\mathbf{n}\,\mathrm{d}S. \tag{16}$$

where primes have been dropped on the dimensionless variables for ease of reading. The Laplace's equation of (13) follows directly from (2). The Dirichlet boundary condition on the solid–liquid interfaces (14) follows from combining (5) and (6). The Neumann boundary condition (15) results from combining (1), (3), and (4). The mean stress expression (16) results from (11) and (5), and $\underline{\underline{\boldsymbol{I}}}$ is the identity tensor. Given a desired macroscopic strain rate $\underline{\underline{\dot{\boldsymbol{e}}}}$, (13), (14), and (15) can be solved to determine c, which can then be substituted into (16) to determine the mean stress that needs to be applied to produce that strain rate.

Another way of writing (16) is in terms of the total stress tensor,

$$\underline{\underline{\overline{\boldsymbol{\sigma}}}} = \phi\underline{\underline{\overline{\boldsymbol{\sigma}}}}^l + (1-\phi)\underline{\underline{\overline{\boldsymbol{\sigma}}}}^s, \tag{17}$$

where ϕ is the porosity (volume fraction of melt). $\phi \equiv V_\mathrm{l}/V_\mathrm{cell}$ where V_l is the volume of liquid melt and V_cell is the volume of a unit cell (when considering a tessellation of unit cells). In the calculations that follow it will be assumed that as porosity varies, the volume of the cell remains fixed. (16) can be written in terms of total stress as

$$\underline{\underline{\overline{\boldsymbol{\sigma}}}} = -P^l\underline{\underline{\boldsymbol{I}}} + \frac{1}{V_\mathrm{cell}}\int c\,\mathbf{x}\,\mathbf{n}\,\mathrm{d}S. \tag{18}$$

Since (13), (14), (15) are linear equations, the vacancy concentration c is linearly related to the strain rate tensor $\underline{\underline{\dot{\boldsymbol{e}}}}$. As a consequence, the results of the calculations can be written in suffix notation as

$$\overline{\sigma}_{ij} = -P^l\delta_{ij} + C_{ijkl}\dot{e}_{kl} \tag{19}$$

where δ_{ij} is the Kronecker delta and C_{ijkl} is the viscosity tensor. It is possible to write a single statement of the problem for this viscosity tensor. The linear relationship between c and $\underline{\underline{\dot{\boldsymbol{e}}}}$ can be written as $c = \gamma_{ij}\dot{e}_{ij}$ where γ_{ij} is a symmetric second rank ten-

sor that satisfies

$$\nabla^2 \gamma_{ij} = 0 \text{ in } V_s, \tag{20}$$

$$\gamma_{ij} = 0 \text{ on } S_{\text{sl}}, \tag{21}$$

$$\frac{\partial \gamma_{ij}}{\partial n} = x_p n_p n_i n_j \text{ on } S_{\text{ss}}, \tag{22}$$

$$C_{ijkl} = \frac{1}{V_{\text{cell}}} \int \gamma_{kl} x_i n_j \, \mathrm{d}S. \tag{23}$$

106 **2.2 Coble (grain-boundary diffusion) creep**

The governing equations for Coble creep are very similar to those outlined above for Nabarro-Herring creep. The only differences that arise from those in section 2.1 are in changes to equations (1), (2), and (3). In Coble creep, diffusion only transports matter on the boundaries of the grains. The corresponding Fick's law becomes

$$\mathbf{j}_{\text{v}} = -D_{\text{v}}^{\text{gb}} \nabla_{\perp} c, \tag{24}$$

where D_{v}^{gb} is the diffusivity of vacancies along the grain boundary, and $\nabla_{\perp}$ is the perpendicular gradient operator, defined by

$$\nabla_{\perp} \equiv (\underline{\underline{\boldsymbol{I}}} - \mathbf{nn}) \cdot \nabla, \tag{25}$$

where $\mathbf{n}$ is the outward normal to the grain. Conservation of mass relates the divergence of the flux to the plating rate

$$\tfrac{1}{2} \Omega \delta \nabla_{\perp} \cdot \mathbf{j}_{\text{v}} = \dot{r}, \tag{26}$$

where δ is the grain boundary thickness. The factor of $1/2$ arises because each grain boundary borders two grains. Note that some authors, such as Takei and Holtzman (2009a), use the symbol δ to denote the grain-boundary half-width. Here δ denotes the full-width, as used by Cocks and Searle (1990) and Raj and Ashby (1971). As before, the plating rate $\dot{r}$ is constant on each planar face of the grain. Combining (26) and (24) leads to a Poisson equation for the concentration of vacancies

$$-\tfrac{1}{2} \Omega \delta D_{\text{v}}^{\text{gb}} \nabla_{\perp}^2 c = \dot{r} \text{ on } S_{\text{ss}}. \tag{27}$$

An additional subtlety arises in Coble creep, in that boundary conditions also need to be specified on the grain edges. When melt is present on the grain edges, this condition is simply that c is constant on the edges. When melt is not present, c must be continuous across the grain edges, and flux must be conserved, which implies that

$$\sum_m \boldsymbol{\nu}_m \cdot \nabla_{\perp} c = 0 \text{ on } \Gamma, \tag{28}$$

where Γ represents the contact line where grain boundaries meet, m is an index identifying each grain boundary, and $\boldsymbol{\nu}_m$ is the outward-pointing co-normal to each surface at the contact line (i.e. $\boldsymbol{\nu}_m$ is perpendicular to both the normal to the surface and a vector in the direction of the contact line).

2.2.1 Scaling

As for Nabarro-Herring creep, the governing equations can be simplified by scaling. The scaling for length and stresses are the same, but (27) motivates a slightly different choice of timescale, $\tau = d^3/\delta D^{\mathrm{gb}}$ where $D^{\mathrm{gb}} = D_{\mathrm{v}}^{\mathrm{gb}} c_0 \Omega$ is the self-diffusion coefficient for grain-boundary diffusion. The natural viscosity scale is then $kTd^3/\delta D^{\mathrm{gb}}\Omega$, proportional to the third power of grain-size. The dimensionless equations are

$$-\nabla_\perp^2 c = 2\left(\mathbf{n}\cdot\underline{\underline{\dot{\boldsymbol{\varepsilon}}}}\cdot\mathbf{n}\right)\mathbf{x}\cdot\mathbf{n} \text{ on } S_{\mathrm{ss}}, \tag{29}$$

$$c = 0 \text{ on } S_{\mathrm{sl}}, \tag{30}$$

$$\overline{\underline{\underline{\boldsymbol{\sigma}}}} = -P^l\underline{\underline{\boldsymbol{I}}} + \frac{1}{V_{\mathrm{cell}}}\int c\,\mathbf{x}\,\mathbf{n}\,\mathrm{d}S. \tag{31}$$

As for Nabarro-Herring creep, we may write $c = \gamma_{ij}\dot{e}_{ij}$ to get a single statement of the problem for the viscosity tensor as

$$-\nabla_\perp^2\gamma_{ij} = 2x_p n_p n_i n_j \text{ on } S_{\mathrm{ss}}, \tag{32}$$

$$\gamma_{ij} = 0 \text{ on } S_{\mathrm{sl}}, \tag{33}$$

$$\sum_m \boldsymbol{\nu}_m\cdot\nabla_\perp\gamma_{ij} = 0 \text{ on } \Gamma, \tag{34}$$

$$C_{ijkl} = \frac{1}{V_{\mathrm{cell}}}\int \gamma_{kl}x_i n_j\,\mathrm{d}S. \tag{35}$$

3 Results

3.1 Nabarro-Herring (volume diffusion) creep

3.1.1 2D: Tiling of hexagons

The simplest and most natural two-dimensional geometry one can consider is a tiling of hexagonal grains. The hexagonal symmetry demands that the fourth-rank viscosity tensor is isotropic, and hence can be described by just two numbers: the shear viscosity η and the bulk viscosity ζ.

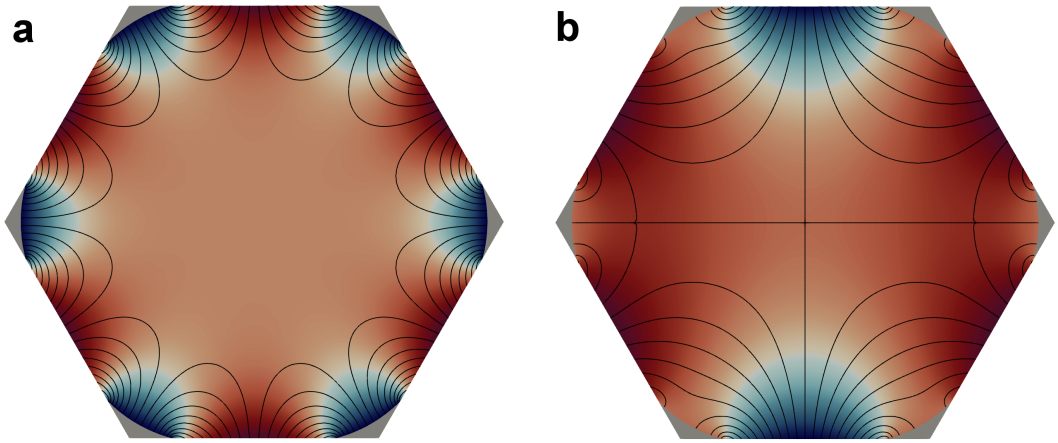

Figure 1. Illustration of the hexagonal unit cell undergoing a) isotropic bulk deformation and b) pure shear. Regions of melt are shown in grey. The colour scale inside the solid grain is used to show concentration of vacancies. Black lines show the paths of vacancy flux. Under bulk compression material is transported from the grain–grain boundaries to the melt pores, resulting in shrinking of the melt pores and overall compaction.

In the absence of melt, only shear is possible, with shear viscosity given in dimensional form as

$$\eta_0 = \frac{kTd^2}{36D\Omega}, \tag{36}$$

where d is the perpendicular distance between opposite sides of the hexagon, and the subscript 0 is used to denote the absence of melt. The dimensional factors in (36) are obtained by scaling, and the numerical prefactor of 1/36 results from a calculation. Remarkably, this numerical prefactor can be obtained from a simple geometrical integral, without the need to explicitly solve Laplace's equation (see appendix A.2 for the derivation). (36) is identical to the formula attributed to Gibbs by Raj and Ashby (1971). A slightly different numerical prefactor for hexagonal grains of 1/30.2 was obtained by Beeré (1976). The 1/36 factor given here is exact, and Beeré (1976)'s results only differ due to approximations he made to the geometry in order to get an analytic expression for the solution of Laplace's equation. The 1/36 prefactor is not that different from that for a circle of diameter d, which is 1/32.

Our principal interest here is the effect of melt on the viscosity, which requires assumptions about how the melt is organised at the grain scale. For the hexagonal tiling we assume that melt lies at the vertices of the hexagons, and takes the form of a tex-

turally equilibrated geometry (minimum surface energy). This implies that the solid–melt interfaces are simply arcs of circles, which meet the solid–solid (grain–grain) contacts at the dihedral angle (German, Suri, and Park (2009)). There are thus two parameters that describe the effect of melt: the porosity (volume fraction of melt) ϕ and the dihedral angle θ.

The geometry of the hexagonal unit cell with melt present is illustrated in Figure 1. The governing equations in (20)-(23) have been solved numerically using the FEniCS software (Logg, Mardal, & Wells, 2012; Logg & Wells, 2010) to obtain the bulk and shear viscosities, presented in Figure 2. Such finite element calculations have been performed previously for circular pores by Cocks (1996), and the calculations here extend Cocks's analysis to a wider range of pore shapes.

Figure 2a shows the bulk viscosity (scaled by the reference shear viscosity η_0 in the absence of melt), which becomes singular as the porosity vanishes. As apparent from the plot, this singularity is logarithmic in the porosity. This singularity arises because very small melt pores act like point sources/sinks of vacancies at the vertices of the hexagon. In two-dimensions, point-source solutions of Laplace's equations are proportional to the logarithm of distance away from the source. Thus at very small porosities, the vacancy concentration grows logarithmically approaching the vertices of the hexagon; this manifests in a logarithmic singularity in the bulk viscosity. The behaviour at small porosity can be obtained formally by matched asymptotics (appendix A.3.1) as

$$\frac{\zeta}{\eta_0} \sim -\frac{9\sqrt{3}}{4\pi}\log\phi - 3.92922 - \frac{9\sqrt{3}}{2\pi}\log\kappa(\theta), \tag{37}$$

which is plotted as the dotted lines in Figure 2. The leading order term, proportional to $\log\phi$, is independent of the shape of melt pores. Hence all curves in Figure 2a approach the same slope as porosity tends towards zero. The melt pore shape affects the next order, constant term, which is expressed in terms of the logarithmic capacity $\kappa(\theta)$ of the pore shape, which in turn depends on the dihedral angle θ. Figure 3 plots the logarithmic capacity $\kappa(\theta)$ calculated using the `capacity` routine of the *Schwarz-Christoffel Toolbox* (Driscoll, 2002; Driscoll & Trefethen, 2002). For a fixed porosity, the bulk viscosity increases with increasing dihedral angle. The full numerical solutions start to depart significantly from the asymptotic solutions once $\phi \gtrsim 0.3\%$. The bulk viscosity vanishes once all the grain boundaries have been wetted, which happens for larger porosities at larger dihedral angles.

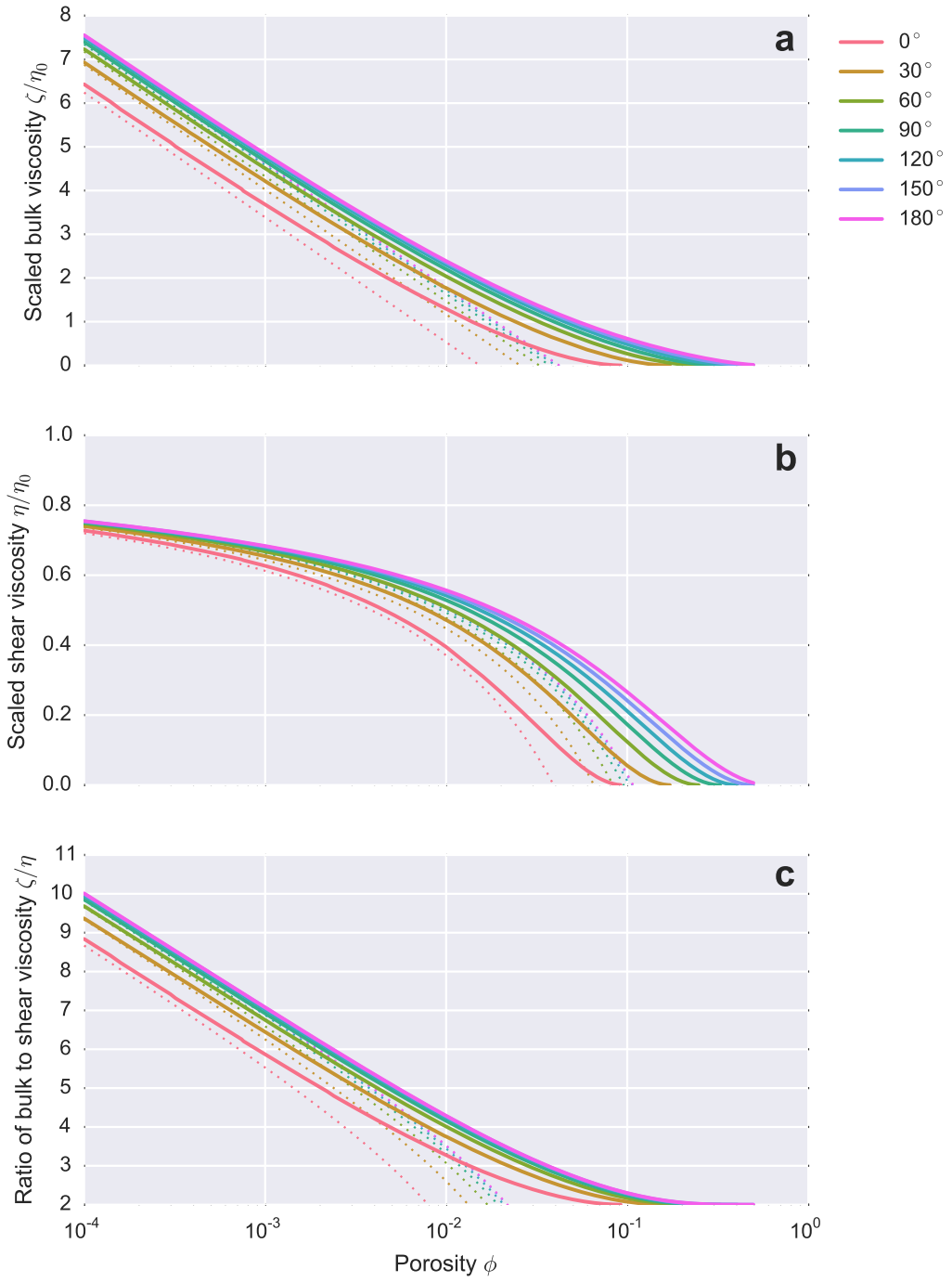

Figure 2. Bulk and shear viscosities for Nabarro-Herring creep of hexagonal grains with melt. Solid lines show the finite element calculations for different dihedral angles as indicated in the legend. Dotted lines show the asymptotic results for small porosity. Porosity is shown on a logarithmic scale on the horizontal axis. On the vertical axes are shown a) scaled bulk viscosity ζ/η_0, b) scaled shear viscosity η/η_0, and c) the ratio of bulk to shear viscosity ζ/η.

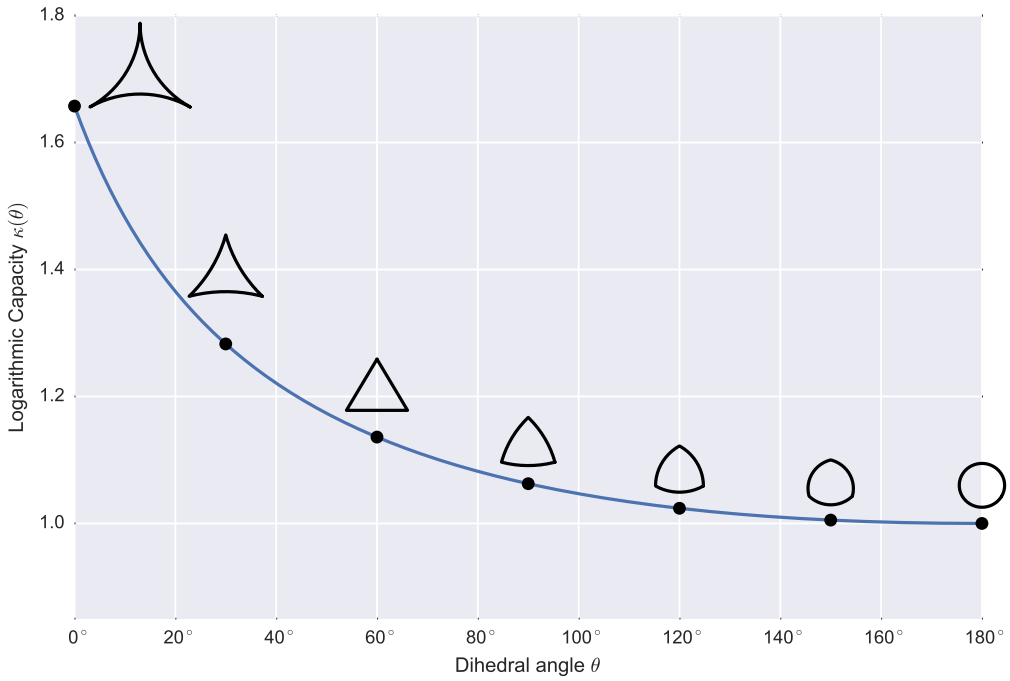

Figure 3. Logarithmic capacity $\kappa(\theta)$ as a function of dihedral angle θ. $\kappa(\theta)$ varies from 1.6574 at zero dihedral angle to 1.0 at 180°. Also shown are the pore shapes for $\theta = 0°$, 30°, 60° (an equilateral triangle), 90°, 120°, 150°, and 180° (a circle). The scaling is such that each pore has the same area, equal to π.

The shear viscosity (again scaled by the reference shear viscosity η_0 in the absence of melt) is plotted in Figure 2b. The shear viscosity is not singular as the porosity vanishes, and tends to η_0. However, just a small amount of melt can cause a notable drop in the shear viscosity – for a 0.1% porosity, the shear viscosity is around 63 to 68% of the melt-free value, depending on the dihedral angle. The approach of the shear viscosity to η_0 as porosity vanishes is proportional to the reciprocal of the logarithm of ϕ. Matched asymptotics (appendix A.3.2) yields the small-porosity expression,

$$\frac{\eta}{\eta_0} \sim 1 + \frac{2\pi F}{\sqrt{3}\left(\log(\epsilon\kappa(\theta)) + 2\pi R\right)} \tag{38}$$

where $F = 0.319889078$ and $R = 0.150237305$ are numerical constants, and ϵ is related to ϕ by

$$\epsilon = \left(\frac{\sqrt{3}\phi}{4\pi}\right)^{1/2}. \tag{39}$$

Similar to the bulk viscosity, at higher porosities the shear viscosity vanishes on wetting of the grain boundaries. Figure 2c shows the ratio ζ/η of bulk to shear viscosity, which also demonstrates a logarithmic singularity at small porosities. At larger porosities the ratio ζ/η tends to 2.

3.1.2 3D: Tessellation of tetrakaidecahedrons

A natural generalisation of the tiling of hexagonal grains in 2D is a tessellation of tetrakaidecahedrons (truncated octahedrons) in 3D. The tetrakaidecahedron has 14 faces, 6 of which are squares, 8 of which are hexagons. In the tessellation, three grains meet along grain edges, and four grains meet at the vertices. The tetrakaidecahedron has cubic symmetry. Unlike in the 2D case of hexagons, this symmetry does not lead to isotropy of the fourth-rank viscosity tensor. However, it does reduce the fourth rank tensor to three independent components, which can expressed in Voigt notation as

$$\begin{pmatrix} C_{1111} & C_{1122} & C_{1133} & C_{1123} & C_{1113} & C_{1112} \\ C_{2211} & C_{2222} & C_{2233} & C_{2223} & C_{2213} & C_{2212} \\ C_{3311} & C_{3322} & C_{3333} & C_{3323} & C_{3313} & C_{3312} \\ C_{2311} & C_{2322} & C_{2333} & C_{2323} & C_{2313} & C_{2312} \\ C_{1311} & C_{1322} & C_{1333} & C_{1323} & C_{1313} & C_{1312} \\ C_{1211} & C_{1222} & C_{1233} & C_{1223} & C_{1213} & C_{1212} \end{pmatrix} = \begin{pmatrix} \zeta + \frac{4}{3}\eta_1 & \zeta - \frac{2}{3}\eta_1 & \zeta - \frac{2}{3}\eta_1 & 0 & 0 & 0 \\ \zeta - \frac{2}{3}\eta_1 & \zeta + \frac{4}{3}\eta_1 & \zeta - \frac{2}{3}\eta_1 & 0 & 0 & 0 \\ \zeta - \frac{2}{3}\eta_1 & \zeta - \frac{2}{3}\eta_1 & \zeta + \frac{4}{3}\eta_1 & 0 & 0 & 0 \\ 0 & 0 & 0 & \eta_2 & 0 & 0 \\ 0 & 0 & 0 & 0 & \eta_2 & 0 \\ 0 & 0 & 0 & 0 & 0 & \eta_2 \end{pmatrix}, \tag{40}$$

for a bulk viscosity ζ and two shear viscosities η_1 and η_2. Here we will define the co-ordinates of the tetrakaidecahedron such that the x, y, and z axes are aligned with the normals to the square faces.

In the absence of melt, only shear deformation is permitted, and the two shear viscosities can be calculated by a geometric integral (appendix A.2) over the grain as

$$\eta_{10} = \frac{23}{1536}\frac{kTd^2}{D\Omega}, \qquad \eta_{20} = \frac{31}{1536}\frac{kTd^2}{D\Omega}, \tag{41}$$

where d is the distance between opposite square faces of the tetrakaidecahedron, and zeros are again used to indicate the absence of melt. The anisotropy is apparent, and can expressed by the Zener ratio $A \equiv \eta_2/\eta_1 = 31/23 \approx 1.35$. Shear is easiest when the principal axes of shear are aligned with the square faces. The Voigt-average over all of the viscosities in (41) is

$$\overline{\eta}_0 \equiv \frac{2}{5}\eta_{10} + \frac{3}{5}\eta_{20} = \frac{139}{7680}\frac{kTd^2}{D\Omega}, \tag{42}$$

and will be used as a reference quantity in what follows. The Voigt-average is obtained by averaging the viscosity tensor C_{ijkl} over all possible orientations of the grain. The numerical prefactor $139/7680 \approx 0.0181$ is reasonably similar to the numerical prefactor for a sphere of diameter d, which is $1/40 = 0.025$ (Herring, 1950). The prefactor $139/7680$ is also similar to another calculation for the tetrakaidecahedron by Shah and Chokshi (1998), which yielded a prefactor of $1/54 = 0.0185$, but that study did not consider the inherent anisotropy of the shape.

In three-dimensions, determining the textural equilibrium melt geometries is rather more involved than in 2D. Such calculations have recently been presented in Rudge (2018), and examples of these melt geometries are shown in Figure 4. Figures 5 and 6 plot the bulk and shear viscosities for a tessellation of tetrakaidecahedral unit cells with melt present, using the calculated geometries of Rudge (2018). The viscosities are again a function of two parameters: the porosity ϕ and the dihedral angle θ. As discussed in Rudge (2018), there are different topologies of the melt network depending on these two parameters. When the dihedral angle is less than 60° and the porosity small, melt lies along the triple lines where three grains meet, and forms a connected network. For small porosities, and dihedral angles greater than 60°, melt resides in isolated pockets and does not form a connected network. The effect of melt on viscosity has only been calculated here for the cases where the melt forms a connected network (so that it is possible to expel melt by compaction).

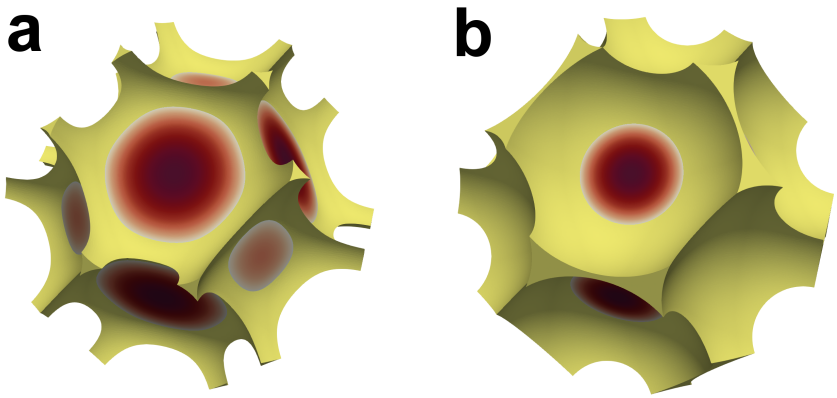

Figure 4. Examples of two melt topologies around tetrakaidecahedral grains. Both examples have a dihedral angle of 30° (Rudge, 2018). a) shows the connected or "c" topology for a porosity of 0.03. b) shows the square-wetted or "s" topology for a porosity of 0.12. The melt network is shown in yellow, and the grain faces are in a colour scale showing vacancy concentration during bulk deformation for Coble creep.

The topology that has melt connected along the grain edges (termed "c" for connected) is shown as thin lines on Figures 5 and 6. At higher porosities, melt starts to wet the square faces of the tetrakaidecahedrons, forming a different melt topology (termed "s" for square-wetted). This topology is shown as the thicker lines on Figures 5 and 6.

For dihedral angles less than 60°, the "c" topologies have a logarithmic singularity in the bulk viscosity. The reason for this logarithmic singularity is similar to the 2D case, with melt tubules acting as line sources/sinks of vacancies along grain edges when the porosity is small. An asymptotic analysis (appendix A.4) yields the small porosity behaviour

$$\frac{\zeta}{\overline{\eta}_0} \sim -\frac{160\sqrt{2}}{139\pi} \log \phi, \tag{43}$$

which is plotted as the black dotted line in Figure 5. The next term in the asymptotic analysis is a constant term, and depends on the details of the melt geometry. This geometry is nontrivial to determine in 3D for an infinitesimal amount of melt. Nevertheless, the leading order term in (43) seems to provide a good match to the slope of the numerical results at low porosity. The slope in 3D (-0.518) is rather less than the slope in 2D (-1.240). More broadly, the predicted variations in the ratio of bulk to shear viscosity are relatively modest, unless the porosity becomes extremely small: ζ/η varies from

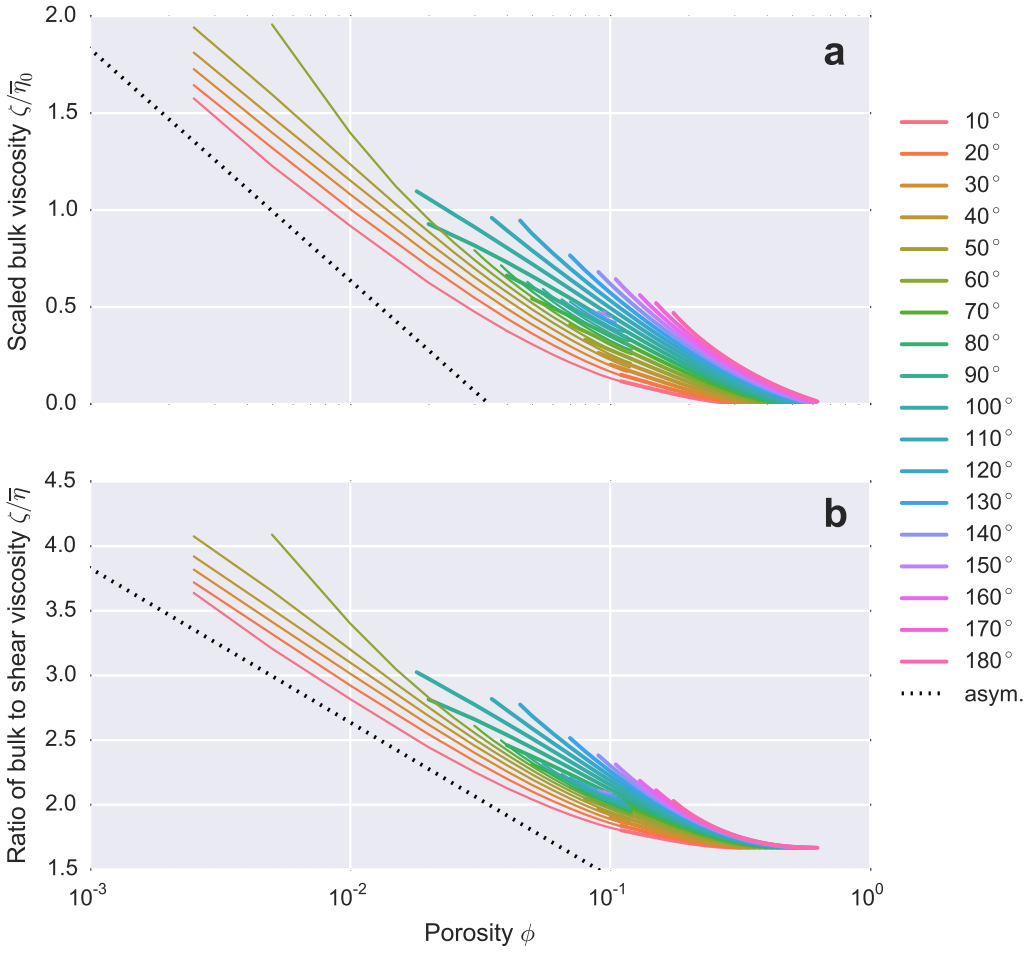

Figure 5. a) Scaled bulk viscosity and b) scaled ratio of bulk to shear as a function of porosity for a tessellation of tetrakaidecahedral unit cells undergoing Nabarro-Herring creep. Thin lines show "c" topologies (connected along the grain edges, Figure 4a), thick lines show "s" topologies (where the square faces are wetted, Figure 4b). The dashed black line shows the expected slope from the asymptotic analysis for small porosities (the intercept of the line has been chosen arbitrarily).

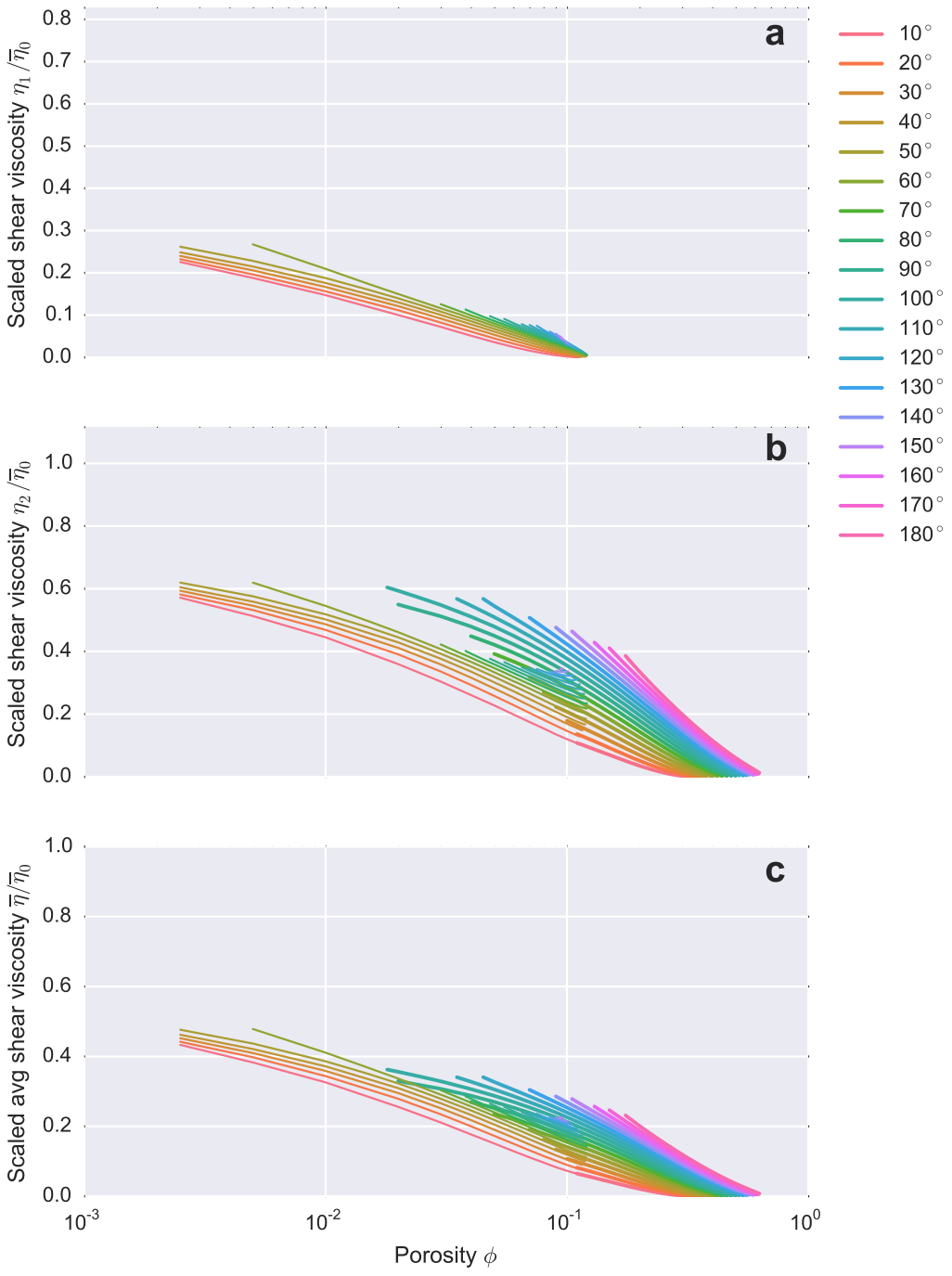

195 **Figure 6.** Scaled shear viscosities as a function of porosity for a tessellation of tetrakaidec-
196 ahedral unit cells undergoing Nabarro-Herring creep. a) $\eta_1/\overline{\eta}_0$, b) $\eta_2/\overline{\eta}_0$, and c) Voigt-average
197 $\overline{\eta}/\overline{\eta}_0$. Lines styles are the same as Figure 5 corresponding to the different topologies of the melt
198 network.

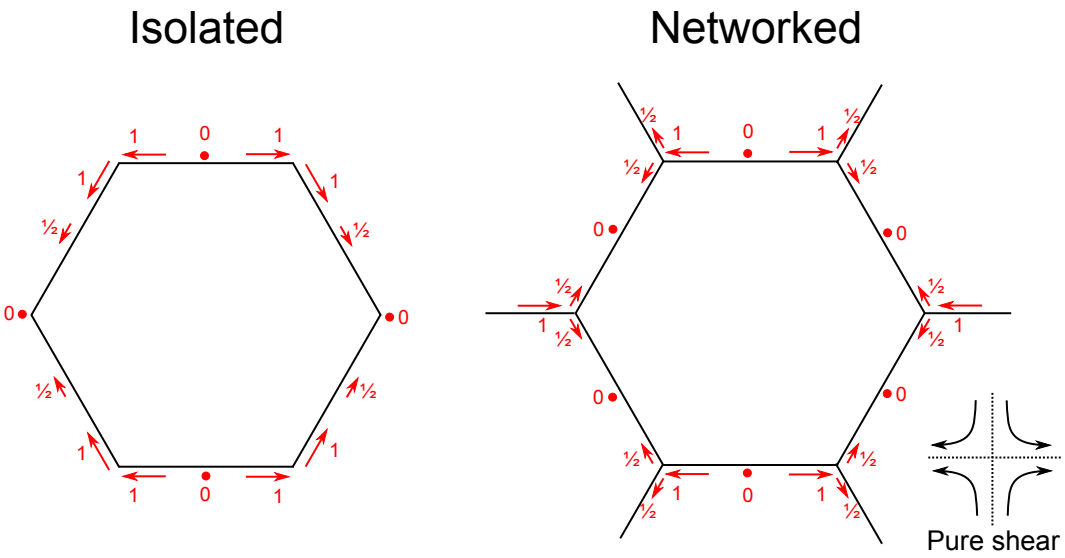

Figure 7. Two distinct conceptual models for Coble creep in the absence of melt for hexagonal grains. On the left is the isolated assumption, where grain boundary diffusion is restricted to an individual grain. On the right is the networked assumption, where matter can be transported from one grain to another through the network of grain boundaries. Pure shear is applied, and shown in red with arrows are the corresponding fluxes of atoms at different locations.

around 4.0 at a porosity of $\phi \sim 10^{-3}$ to a limiting value of $5/3 \approx 1.67$ at higher porosities.

Figure 6 plot the shear viscosities, both the individual η_1 and η_2, along with the Voigt-average $\overline{\eta} = \frac{2}{5}\eta_1 + \frac{3}{5}\eta_2$. One notable feature of this plot is the vanishing of η_1 when wetting of the square faces occurs. The presence of melt along the square faces allows easy shearing in pure shear with principal axes aligned with the normals to the square faces. The general trend of shear viscosity against porosity for small porosity is similar to that seen in 2D. However, there is a greater overall reduction in the shear viscosity with porosity. For example, even a small porosity of 0.1% is expected to have a Voigt-average shear viscosity approximately half that of the melt-free value.

3.2 Coble (grain-boundary diffusion) creep

3.2.1 2D: Tiling of hexagons

Analysis of Coble creep is generally simpler than that of Nabarro-Herring creep, because diffusion takes place over manifolds of dimension one lower than that of the space

(e.g. over lines in 2D, planes in 3D). Coble creep in the absence of melt for hexagonal grains is illustrated in Figure 7. An additional subtlety arises for Coble creep, in that the shear viscosity one obtains depends crucially on assumptions about what happens at the triple points where three grains meet. Two possible assumptions are shown in Figure 7: In the first case, the grain is considered isolated, and grain-boundary diffusion is restricted to an individual grain (this is the assumption made by Takei and Holtzman (2009a)). In the second case, it is assumed that all grain boundaries are connected such that matter can be transported from one grain to neighbouring grains through the network of grain boundaries (this is the assumption made by Spingarn and Nix (1978)). When considering a tessellation of identical grains, it is more reasonable to make the networked assumption as there is no physical process that would be expected to restrict diffusion to an individual grain.

If the grain is assumed isolated, the shear viscosity is given by (appendix B.1)

$$\eta_{0,\text{isolated}} = \frac{7}{432}\frac{kTd^3}{\delta D^{\text{gb}}\Omega}, \tag{44}$$

where d is the distance between opposite sides of the hexagon. The numerical prefactor of $7/432 \approx 0.0162$ is very similar to that for a circle of diameter d, which is $1/64 \approx 0.0156$ (Takei & Holtzman, 2009a). When the grain-boundaries are networked, the viscosity is significantly less, and is given by

$$\eta_{0,\text{networked}} = \frac{1}{144}\frac{kTd^3}{\delta D^{\text{gb}}\Omega}, \tag{45}$$

as found by Spingarn and Nix (1978). The viscosity for the networked case is lower by a factor of $3/7 \approx 0.43$. Under the networked assumption, each vertex of the hexagon is identical, and therefore must be at the same chemical potential (note that each of the triple junctions in Figure 7 has the same pattern of fluxes). The vertices are not identical in the isolated case, where the four vertices at the top and bottom of the hexagon in Figure 7 are at a different chemical potential to the two on the far left and right. The networked case is weaker because there is a shorter effective diffusion distance from one part of the hexagon to another, provided by the "short-circuiting" at the triple points.

Takei and Holtzman (2009a) and Holtzman (2016) have argued that the presence of a very small amount of melt can radically reduce the shear viscosity. They argue this is due to the "short-circuiting" nature of the melt, which acts as a fast path for diffusion. Whether such a reduction is seen for the hexagonal configuration here depends on

whether the "isolated" or "networked" assumption is made for the situation without melt. In fact, adding an infinitesimal amount of melt at the triple junctions of the networked example makes no difference, because all triple junctions are already at the same chemical potential. Hence in this case there is no weakening effect of a small amount of melt. However, if the situation without melt is assumed isolated, then there is a drop by a factor of 3/7 when melt is introduced.

The effect of melt pores on a hexagonal array of grains has been discussed by Cocks and Searle (1990), who find for the same geometry of melt pores as depicted in Figure 1 that

$$\frac{\eta}{\eta_{0,\text{shorted}}} = \left(\frac{A_{\text{ss}}}{A_{\text{cell}}}\right)^3 \tag{46}$$

where $A_{\text{ss}}/A_{\text{cell}}$ is the fraction of the boundary of the unit cell that is grain–grain contact ($A_{\text{ss}} = A_{\text{cell}}$ with no melt present, $A_{\text{ss}} = 0$ when complete wetting occurs). $\eta_{0,\text{shorted}}$ is the viscosity in the presence of an infinitesimal amount of melt, equal to the networked result given in (45). The fraction $A_{\text{ss}}/A_{\text{cell}}$ is related to porosity ϕ and dihedral angle θ by an expression of the form

$$\frac{A_{\text{ss}}}{A_{\text{cell}}} = 1 - \sqrt{\frac{\phi}{\phi_d(\theta)}} \tag{47}$$

where $\phi_d(\theta)$ is the porosity at which disaggregation occurs (i.e. complete wetting of the grain boundaries). $\phi_d(\theta)$ as a function of dihedral angle is given explicitly in appendix B.2.1. Hence

$$\frac{\eta}{\eta_{0,\text{shorted}}} = \left(1 - \sqrt{\frac{\phi}{\phi_d(\theta)}}\right)^3, \tag{48}$$

which is plotted in Figure 8. Once melt is present, bulk deformation is possible. Owing to a symmetry of the governing equations known as the Cauchy relation, bulk and shear viscosity are linked by $\zeta = 2\eta$ in 2D (see appendix B.2). As consequence, both bulk and shear viscosity show the same behaviour with porosity for Coble creep.

3.2.2 3D: Tessellation of tetrakaidecahedrons

As in 2D, the viscosity of tetrakaidecahedrons in 3D depends on assumptions about the behaviour at the triple lines where three grains meet. Figure 9 depicts three possibilities: 1, Isolated, where grain-boundary diffusion is restricted to an individual grain; 2, Networked, where the grain shown is one grain of an infinite tessellation of grains, and grain-boundary diffusion can move matter from one grain to neighbouring grains; 3, Shorted, where an infinitesimal amount of melt is assumed to lie along the grain edges forming

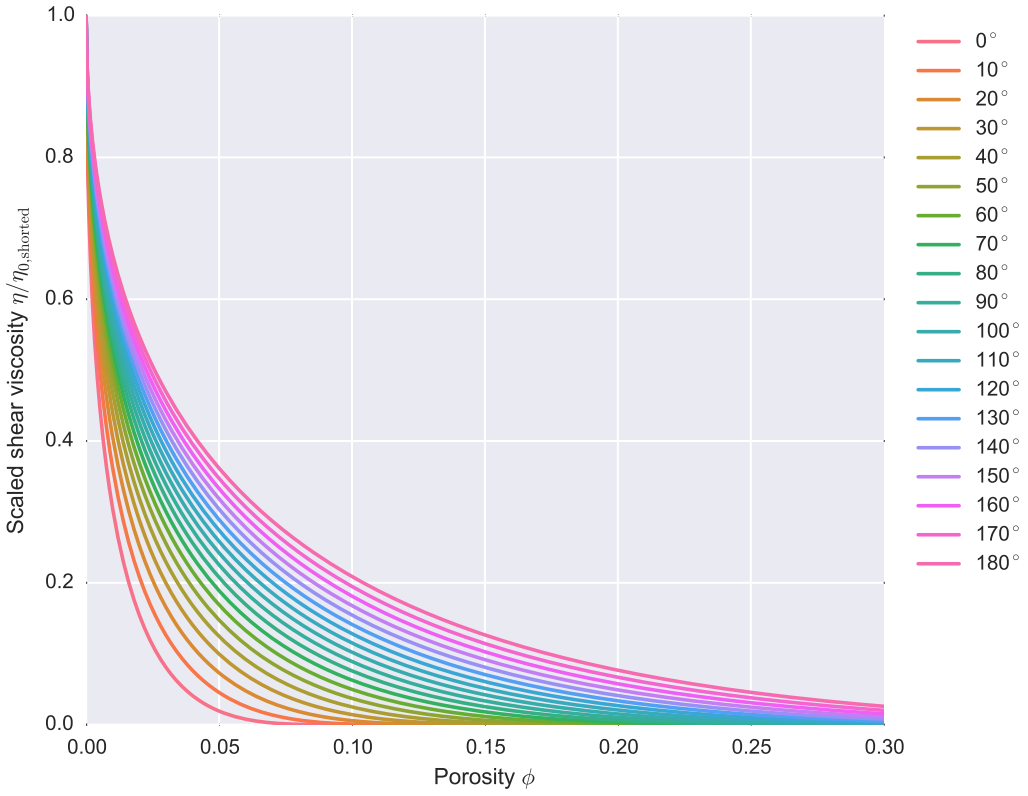

Figure 8. Scaled shear viscosity plotted against porosity for hexagonal grains undergoing Coble creep.

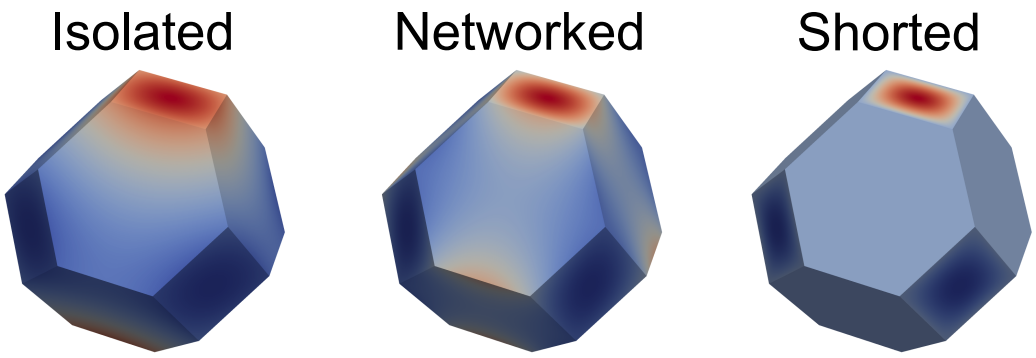

Figure 9. Vacancy concentrations under pure shear for Coble creep of tetrakaidecahedrons with three different assumptions (isolated, networked, or shorted). The principal axes of shear are aligned with the square faces of the tetrakaidecahedron.

	η_{10}	η_{20}	$\overline{\eta}_0$
isolated	0.0043178	0.0077000	0.0063471
networked	0.0012242	0.0034715	0.0025726
shorted	0.0005491	0.0026965	0.0018376

Table 1. Shear viscosities of tetrakaidecahedrons for Coble creep under three different assumptions (isolated, networked, shorted). The numerical prefactors above should be multiplied by $kTd^3/\delta D^{\mathrm{gb}}$ to give the dimensional viscosity.

a fast path for diffusion. The corresponding viscosities for these three situations are given in Table 1. The numerical prefactor for the Voigt-average viscosity for the isolated case, 0.0063471, is fairly similar to that for a sphere of diameter d, which is $1/120 \approx 0.0083333$ (Takei & Holtzman, 2009a). The anisotropy in viscosity is larger than seen for Nabarro-Herring creep, with Zener ratios η_2/η_1 given by 1.78, 2.84, and 4.91 for the three cases.

As in 2D, the networked configuration has a significantly reduced viscosity compared to the isolated configuration (in terms of the Voigt-average, the viscosity is reduced by a factor of 0.40, a similar factor to that seen for the hexagonal case). A key difference is that in 3D, unlike in 2D, the shorted and networked configurations are not identical. The shorted configuration reduces the viscosity by a factor of 0.71 compared to the networked configuration, and is a factor of 0.29 lower than the isolated configuration.

The effect of melt on the viscosities is plotted in Figure 10. The anisotropy is clear, and arises largely from the smaller contact areas of the square faces compared to the hexagonal faces. As for Nabarro-Herring creep, the shear viscosity η_1 vanishes when the square faces become wetted. Owing to the Cauchy relation symmetry, the bulk viscosity is a constant multiple of the Voigt-average shear viscosity, given by $\zeta = \frac{5}{3}\overline{\eta}$ (appendix B.2).

The main behaviour of viscosity as a function of porosity in 3D for Coble creep can be understood from the simple theory developed by Cooper and Kohlstedt (1984, 1986) and Takei and Holtzman (2009a). In the study by Takei and Holtzman (2009a) the grain geometry is simplified to be a sphere with circular contact patches. With these simplifications, the shear viscosity with melt present can be related to the area of solid–solid

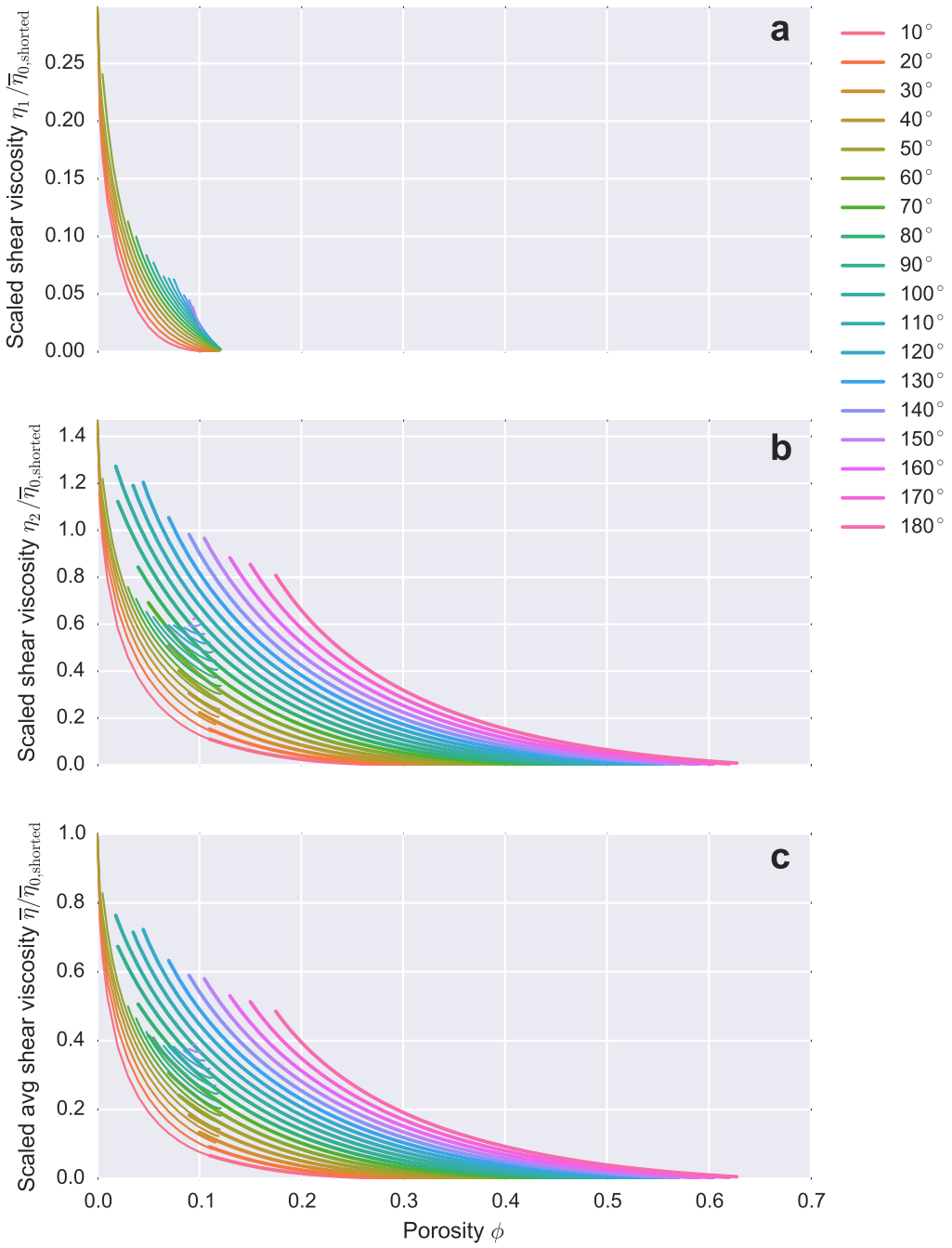

Figure 10. Scaled shear viscosities plotted against porosity for Coble creep of tetrakaidecahedrons. Line styles are as in Figure 5. a) shows $\eta_1/\overline{\eta}_0$, which vanishes when the square faces become wetted. b) shows $\eta_2/\overline{\eta}_0$, and c) shows the Voigt-average $\overline{\eta}/\overline{\eta}_0$. The scaling has used the "shorted" reference value from Figure 1. Note that this plot only shows values with melt present ($\phi > 0$), and not the potential jump in shear viscosity at the onset of melting.

contact by

$$\frac{\overline{\eta}}{\eta_{0,\text{shorted}}} \approx \left(\frac{A_{\text{ss}}}{A_{\text{cell}}}\right)^2, \tag{49}$$

where $A_{\text{ss}}/A_{\text{cell}}$ is the fraction of the boundary of the unit cell that is grain–grain contact. The exact relationship between shear viscosity and contact areas for the more complex geometry considered here is given in appendix B.2, and is a weighted sum of squares of the individual contact areas. The expression above does not take account of the differences between the different contacts (i.e. the differences in both shape and area of the square and hexagonal contacts, and the differences in distances of the contacts from the grain center). Nevertheless, (49) provides a useful approximation. In turn, the contact areas can be approximately related to porosity by

$$\frac{A_{\text{ss}}}{A_{\text{cell}}} \approx 1 - \sqrt{\frac{\phi}{\phi_d(\theta)}} \tag{50}$$

where $\phi_d(\theta)$ is a function of dihedral angle (Rudge, 2018; von Bargen & Waff, 1986). This is a good approximation for a tube-like melt geometry (see (B14) of Rudge (2018)). Hence for $\phi > 0$ (Takei & Holtzman, 2009a)

$$\frac{\overline{\eta}}{\eta_{0,\text{shorted}}} \approx \left(1 - \sqrt{\frac{\phi}{\phi_d(\theta)}}\right)^2, \tag{51}$$

which differs from the 2D result in (48) only in the exponent of 2 rather than 3.

The broad validity of the approximation in (51) is illustrated in Figure 11, which plots the square root of the scaled shear viscosity against the square root of porosity. On this plot, an expression of the form (51) should give a straight line. Certainly for low porosities and connected topologies, the approximation appears to be good. For a 40° dihedral angle typical of basaltic melts, and porosities less than 10%, this implies a ϕ_d of around 0.24 (just slightly larger than ϕ_d of $2.3^{-2} \approx 0.19$ suggested by Takei and Holtzman (2009a) for the olivine–basalt system). Unlike the 2D case, ϕ_d now does not represent exactly the porosity at which disaggregation occurs, because the relationship in (51) is only approximate. Instead ϕ_d represents where disaggregation would be expected to occur if one extrapolates the approximate linear relationship seen at low porosities in Figure 11 to higher porosities.

The full calculations show that the shear viscosity η_2 is proportional to the areas of the hexagonal contacts squared, and η_1 the same for the square contacts (appendix B.2). Thus the main trends in Figure 10a and b mimic those in Figures 16 and 17 of Rudge (2018) which plot the relevant areas against porosity.

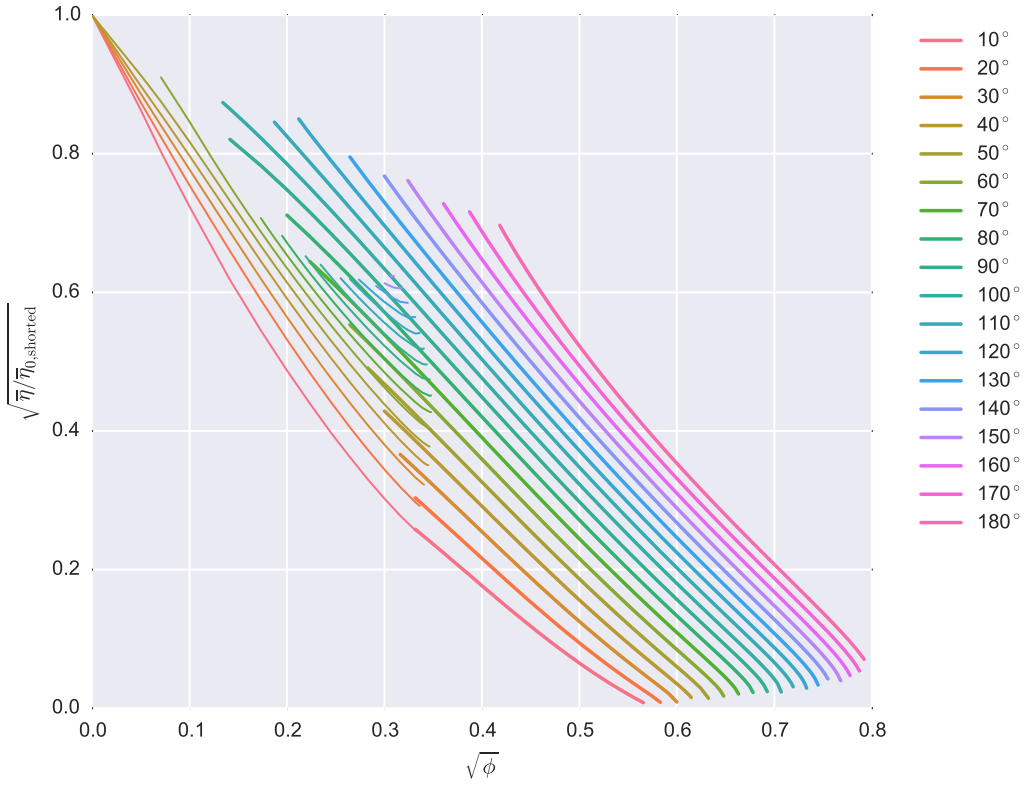

Figure 11. A plot of the same data for Coble creep of tetrakaidecahedrons as in Figure 10c, except axes now show the square root of scaled, Voigt-average shear viscosity against the square root of porosity to reveal a near-linear trend.

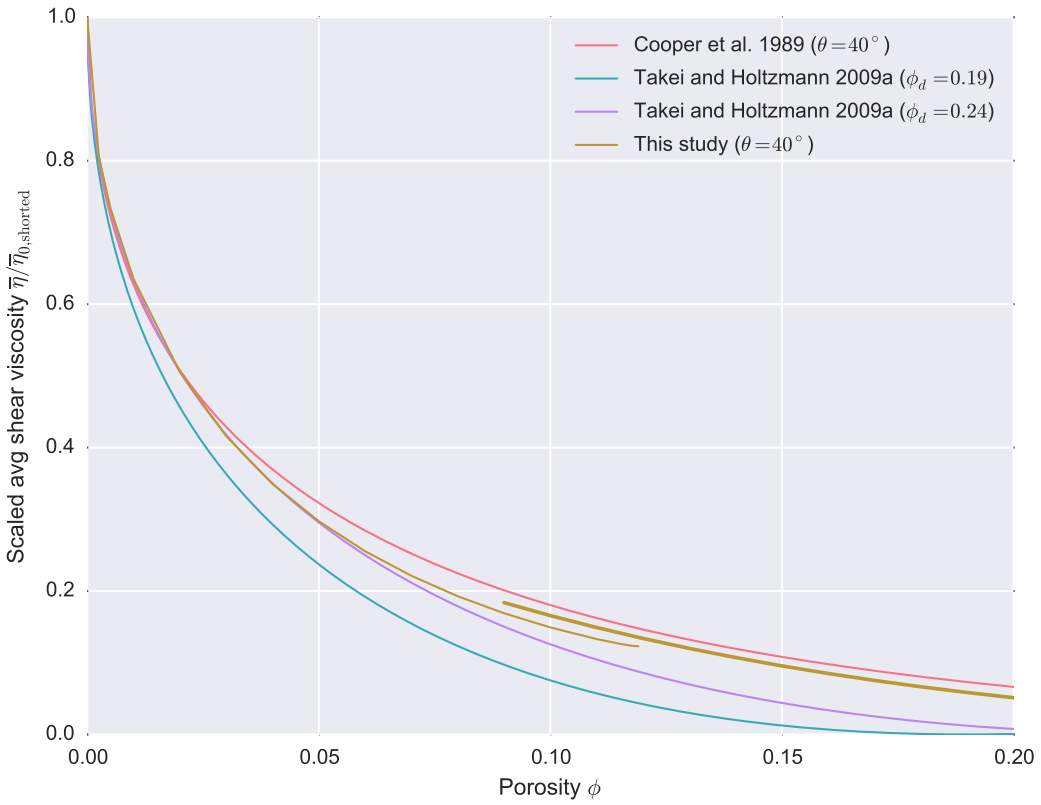

Figure 12. Scaled average shear viscosity against porosity for Coble creep of tetrakaidecahedrons as in Figure 10c, but just showing the results for a dihedral angle of 40°. Also shown are three alternative model curves. The first is given by equations 5, 6, and 7 of Cooper et al. (1989) for a dihedral angle of 40°. The other two curves show the approximate law given by Takei and Holtzman (2009a) and (51) of this manuscript, with two choices of ϕ_d.

The broad agreement of the Coble creep calculations presented here with those of previous studies is illustrated in Figure 12. Shown in the figure is the calculated variation in average shear viscosity for a dihedral angle of 40°, along with model curves from the studies of Takei and Holtzman (2009a) and Cooper et al. (1989). The curves marked Takei and Holtzman (2009a) are given by equation (51), where two values of ϕ_d are shown. The first ($\phi_d = 0.19$) is that directly suggested by Takei and Holtzman (2009a) as appropriate for olivine-basalt; the second ($\phi_d = 0.24$) is the value which better fits the creep calculations presented here for a dihedral angle of 40° at small porosities. With the appropriate choice of ϕ_d the law given in (51) clearly provides a very good approximation to the numerical calculations up to porosities of about $\phi \sim 0.1$, as can also be seen in the near linear nature of the curves in Figure 11 up to $\sqrt{\phi} \sim 0.3$. The departure of the calculations here from the approximate law of (51) arises from the assumption of an isotropic grain model by Takei and Holtzman (2009a), whereas the model here has considerable anisotropy arising from the differences between the square and hexagonal contacts.

Figure 12 also shows the expected behaviour from the model of Cooper et al. (1989), which closely approximates the calculations presented here for a wide range of porosities. The model of Cooper et al. (1989) is also based on tetrakaidecahedrons, but the geometry is simplified by assuming that melt lies in uniform tubes along the grain edges. Cooper et al. (1989) argue that the dominant contribution to the average shear viscosity comes from the hexagonal faces, and thus approximate that the viscosity scales with the fourth power of the distance from the centre of a hexagonal face to the melt. This is a reasonable approximation to have made – while we have shown here that the average shear viscosity depends on a weighted sum of squares of the areas of both the square and hexagonal contacts, it is indeed the hexagonal contacts that form the dominant contribution. For example, in the absence of melt, the hexagonal faces contribute 88% of the total sum in the estimation of the average shear viscosity. The remaining differences between the Cooper et al. (1989) calculations and the model presented here arise due to the more accurate computation of the melt geometry here (i.e. not approximating by tubes), and the direct calculation of the contributions from both the square and hexagonal faces.

4 Discussion

Perhaps the most useful outcome of this work is the expressions relating the bulk and shear viscosities to porosity, given for Coble creep by (51), and for Nabarro-Herring creep by (A.63) and (A.64) in appendix A.5. These expressions can be used in larger-scale geodynamic calculations, such as those models based on the compaction equations of McKenzie (1984).

There are important differences between the rheological laws proposed here and those in common use by the geodynamics community. Perhaps the most important difference concerns the bulk viscosity. Here, the bulk viscosity either has a logarithmic singularity at small porosity (Nabarro-Herring creep), or is a constant multiple of the shear viscosity (Coble creep). In large-scale geodynamic models, bulk viscosity is usually given by a law with a singularity proportional to $1/\phi$ (e.g. Bercovici, Ricard, and Schubert (2001); Hewitt and Fowler (2008); Schmeling, Kruse, and Richard (2012); Scott and Stevenson (1986); Simpson, Spiegelman, and Weinstein (2010); Sleep (1988)). The reason these studies have a different singular behaviour is ultimately due to a different conception of the physics at the scale of individual grains. In these studies, the grain itself is treated as a Newtonian viscous fluid, so that the governing equations at the microscale are those of Stokes flow. In the present study, the physics of the individual grain is described in terms of diffusion. As shown in section 2, only at the macroscale does the medium act like a Newtonian viscous fluid. The different singular behaviour at small porosity is ultimately a consequence of the different PDEs that are solved at the grain scale: here, Laplace's or Poisson's equation; in the previous studies, Stokes flow. The rheological laws determined here are likely to better represent the viscosities of partially molten rocks because they better reflect the true microscale physics.

In fact, a logarithmic singularity of the bulk viscosity was originally advocated by McKenzie (1984) (see his Figure 6 and (C12)). His equation (C12) arises from a model of Coble creep with spherical pores, as discussed by Arzt et al. (1983) and Pan and Cocks (1994). Here, the results for Coble creep do not show a logarithmic singularity, and this is due to the different melt geometry – here melt lies in tubes along the grain edges for dihedral angles less than 60°, whereas Arzt et al. (1983)'s model assumes spherical pores.

Another key point of difference from previous studies is the effect of a very small amount of melt on the shear viscosity. Takei and Holtzman (2009a) argued that during

Coble creep the shear viscosity is 20% that of the melt-free case when a small amount of melt is present, due to the short-circuiting effect of the melt pathways. The results here suggest the effect of the short-circuiting may be much more modest, since even in the absence of melt, diffusion may be able to take place through the complete network of grain boundaries rather than being restricted to a single grain as Takei and Holtzman (2009a) assume. For Coble creep, the shear viscosity with a very small amount of melt is then 71% of the melt-free value. During Nabarro-Herring creep there is no sudden drop in the shear viscosity at the onset of melting, but there is a very rapid decrease as the porosity increases: At just 0.1% porosity the shear viscosity is halved from the melt-free value. Experimental studies have produced mixed results as to whether there is a sudden drop in the shear viscosity at the onset of melting. Drops in the shear viscosity have been reported for both the organic borneol system (McCarthy & Takei, 2011) and olivine-basaltic melt systems (Faul & Jackson, 2007), but more recent work on borneol has not identified a drop (Yamauchi & Takei, 2016).

It is important to bear in mind the simplifications that have made in this study. Importantly, there has been no exploration here of the effects of chemistry, which is likely to play an important role in the polyphase, polycrystalline, partially molten mantle. Here all crystals have been treated as being the same phase, and all grain-boundaries are those between identical grains. In a polyphase system, there are a series of different grain boundaries depending on the combinations of different mineral phases that meet (Ford & Wheeler, 2004). Thus matter may be transported more easily across some boundaries than others. This may mean that the short-circuiting effect of melt might be greater in a polyphase system than one with a single solid phase. Moreover, each grain-boundary has been treated as freely slipping, and the calculations here could be extended by considering a finite viscosity for the grain boundaries (Lifshitz, 1963). The inclusion of grain boundary viscosity will be particularly important for modelling short-timescale transient deformation (e.g. that associated with seismic attenuation). However, the freely-slipping assumption is likely to be good for modelling the long-timescale deformation associated with mantle convection and melt transport.

The melt geometries on which this study is based are textural equilibrium geometries assuming isotropic surface energies. Anisotropy is likely to play an important role in wetting some grain boundaries, and in turn reducing the shear viscosity. Moreover, the geometry of the melt network must evolve with finite deformation, and more work

needs to be done to explore with interactions between effective rheology and finite deformation.

This study is also based on an assumption of an infinite diffusivity in the melt phase. Finite melt diffusivity will mean the effect of melt-weakening is not as strong as calculated here. The effect of finite diffusivity has been explored by Takei and Holtzman (2009b), and similar calculations could be performed for the more complex geometries considered here. As Takei and Holtzman (2009b) point out, the effects of finite melt diffusivity are most important at very small porosities. Moreover, at large porosities, the rheological laws produced here will also breakdown as they do not consider the finite viscosity of the melt phase. At very large porosities one has a suspension of isolated crystals within a melt, which is described by a very different rheological law.

The precise behaviour of bulk viscosity as a function of porosity can have important consequences for larger-scale dynamics. An important example of this has been given recently by Rees Jones and Katz (2018) and concerns the reaction-infiltration instability (RII), an instability that may be responsible for localising melt transport during mantle melting. Rees Jones and Katz (2018) have demonstrated that a bulk viscosity which varies strongly with porosity is more likely to suppress the RII than one which does not.

The rheological laws derived here have consequences for the rate at which melt bands develop during shear (Holtzman, Groebner, Zimmerman, Ginsberg, & Kohlstedt, 2003; Spiegelman, 2003; Stevenson, 1989). Linear stability analysis shows that melt bands are expected to initially grow at a rate proportional to a weakening factor $\alpha = \mathrm{d}\log\eta/\mathrm{d}\phi$ (Spiegelman, 2003; Stevenson, 1989), which is plotted as a function of porosity for the rheologies considered here in Figure 13. Modelling work on this instability (e.g. Bercovici and Rudge (2016); Katz, Spiegelman, and Holtzman (2006); Rudge and Bercovici (2015); Takei and Katz (2015)) has typically used an empirical rheological law of the form $\eta \propto \exp(\alpha\phi)$, with constant $\alpha \sim -26$, based on a fit to experimental data by Mei et al. (2002). As pointed out by Takei and Holtzman (2009a) for Coble creep, the microscale calculations predict a weakening factor α which varies with porosity. For porosities around 3% as used in experiments (Holtzman et al., 2003), a weakening factor around $\alpha = -17$ is predicted for Coble creep (Figure 13). The growth-rate of melt bands also depends on the ratio of bulk to shear viscosity. The rheological laws here suggest the bulk viscosity is comparable in magnitude to the shear viscosity, as also recently argued by Al-

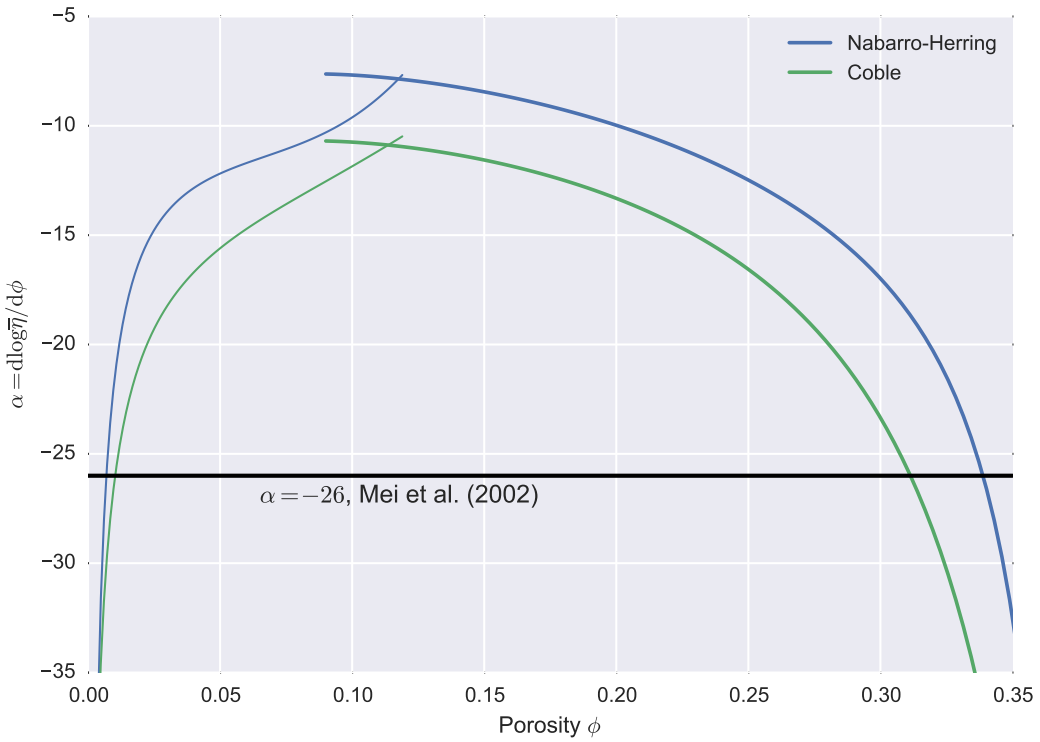

Figure 13. A plot of the porosity-weakening exponent $\alpha = \mathrm{d}\log\overline{\eta}/\mathrm{d}\phi$ against porosity for Nabarro-Herring and Coble creep and a dihedral angle of 40°. The thin lines shows the connected "c" topology and the thick lines the square-wetted "s" topology. Shown as a black horizontal line is the corresponding result for the empirical exponential law proposed by Mei et al. (2002).

isic, Rhebergen, Rudge, Katz, and Wells (2016) on the basis of a comparison of numerical models of melt bands with the laboratory experiments by Qi, Zhao, and Kohlstedt (2013). A bulk viscosity comparable to the shear viscosity was also inferred in four-point bending experiments by Cooper (1990), who found $\zeta/\eta = 1.9$, not too dissimilar the value of $\zeta/\eta = \frac{5}{3} = 1.67$ predicted for Coble creep.

5 Conclusions

This study represents one step towards a better understanding of the rheology of partially molten materials. The effective viscosity tensor has been obtained as a function of porosity and dihedral angle for diffusion creep, both assuming body diffusion (Nabarro-Herring creep) and surface diffusion (Coble creep). The 3D calculations were based on an assumption of a melt geometry that is in textural equilibrium, with a tessellation of identical tetrakaidecahedral (truncated octahedral) unit cells. For Coble creep, the bulk viscosity was shown to be a constant multiple of the shear viscosity, whereas Nabarro-Herring creep has a logarithmic singularity in the bulk viscosity for small porosities. An important challenge for the future is to develop a model of finite deformation which allows the melt geometry to evolve with time, and to be out of textural equilibrium. An additional challenge is to explore other forms of deformation, such as dislocation creep. Such models will undoubtedly provide important insights into the dynamics of melt extraction from the Earth's mantle.

Acknowledgements

The ideas for this work arose out of the 2016 "Melt in the Mantle" programme at the Isaac Newton Institute for Mathematical Sciences. I am grateful to many of the participants of that programme for useful discussions, but particularly grateful to Yasuko Takei and Dan McKenzie for introducing me to the microscale physics of diffusion creep. I am also grateful to David Rees Jones, David Kohlstedt, Richard Katz, and an anonymous reviewer for their comments that helped improve this manuscript. "Melt in the Mantle" was supported by EPSRC Grant Number EP/K032208/1. I am also very grateful to the Leverhulme Trust for support. Data tables of the computed viscosities can be found in the supporting information. Code for generating the textural equilibrium geometries is available at `https://www.johnrudge.com/melt/`.

A Nabarro-Herring creep analytical solutions

A.1 Decomposition into trace and symmetric trace-free components

It is helpful to decompose equations (20-23) for Nabarro-Herring creep into trace and symmetric trace-free components, by writing γ_{ij} as

$$\gamma_{ij} = \frac{\gamma}{N}\delta_{ij} + \tilde{\gamma}_{ij} \tag{A.1}$$

where the symbol γ without subscripts is used to represent the trace part ($\gamma \equiv \gamma_{kk}$), and $\tilde{\gamma}_{ij}$ is the symmetric trace-free part ($\tilde{\gamma}_{kk} = 0$). N is the dimension of the space ($N = 2$ for the hexagons, $N = 3$ for the tetrakaidecahedrons). The trace part of the decomposition is associated with bulk deformation, and the symmetric trace-free part is associated with shear.

The viscosity tensor can be decomposed as

$$C_{ijkl} = B_{ij}\delta_{kl} + \tilde{C}_{ijkl}, \tag{A.2}$$

where the tensors B_{ij} and $\tilde{C}_{ijkl}$ can be obtained from two separate problems, one for bulk deformation:

$$\nabla^2\gamma = 0 \text{ in } V_s, \tag{A.3}$$

$$\gamma = 0 \text{ on } S_{\mathrm{sl}}, \tag{A.4}$$

$$\frac{\partial\gamma}{\partial n} = x_p n_p \text{ on } S_{\mathrm{ss}}, \tag{A.5}$$

$$B_{ij} = \frac{1}{NV_{\mathrm{cell}}}\int \gamma x_i n_j \,\mathrm{d}S, \tag{A.6}$$

and one for shear:

$$\nabla^2\tilde{\gamma}_{ij} = 0 \text{ in } V_s, \tag{A.7}$$

$$\tilde{\gamma}_{ij} = 0 \text{ on } S_{\mathrm{sl}}, \tag{A.8}$$

$$\frac{\partial\tilde{\gamma}_{ij}}{\partial n} = x_p n_p \tilde{N}_{ij} \text{ on } S_{\mathrm{ss}}, \tag{A.9}$$

$$\tilde{C}_{ijkl} = \frac{1}{2V_{\mathrm{cell}}}\int \tilde{\gamma}_{kl}\frac{\partial\tilde{X}_{ij}}{\partial n} \,\mathrm{d}S. \tag{A.10}$$

The tensors $\tilde{N}_{ij}$ and $\tilde{X}_{ij}$ are the trace-free parts of the outer product of the normal vector $\mathbf{n}$ with itself, and the position vector $\mathbf{x}$ with itself respectively, i.e.

$$\tilde{N}_{ij} \equiv n_i n_j - \frac{\delta_{ij}}{N}, \tag{A.11}$$

$$\tilde{X}_{ij} \equiv x_i x_j - x_p x_p \frac{\delta_{ij}}{N}. \tag{A.12}$$

Note that (23) has been simplified to (A.10) using the identity

$$n_i x_j + n_j x_i = \frac{\partial}{\partial n}\left(x_i x_j\right). \tag{A.13}$$

508 ***A.1.1 Isotropy***

For situations where the fourth-rank tensor C_{ijkl} is isotropic, the expressions in (A.6) and (A.10) can be simplified further and written in terms of bulk (ζ) and shear (η) viscosities. Assuming isotropy, the tensors B_{ij} and $\tilde{C}_{ijkl}$ can be written as

$$B_{ij} = \zeta \delta_{ij}, \tag{A.14}$$

$$\tilde{C}_{ijkl} = \eta\left(\delta_{ik}\delta_{jl} + \delta_{il}\delta_{jk} - \frac{2}{N}\delta_{ij}\delta_{kl}\right), \tag{A.15}$$

where expressions for the bulk and shear viscosities can be simplified to

$$\zeta = \frac{1}{N^2 V_{\text{cell}}} \int \gamma x_k n_k \, \mathrm{d}S, \tag{A.16}$$

$$\eta = \frac{1}{2V_{\text{cell}}(N+2)(N-1)} \int \tilde{\gamma}_{kl} \frac{\partial \tilde{X}_{kl}}{\partial n} \, \mathrm{d}S, \tag{A.17}$$

509 using the relationship $\tilde{C}_{klkl} = \eta(N+2)(N-1)$ from (A.15).

510 **A.2 Pure solid**

When the melt phase is absent, the equations of Nabarro-Herring creep simplify considerably. Only shear deformation is permissible, and hence it suffices to consider only the problem for $\tilde{C}_{ijkl}$, which is given by (A.7-A.10). The boundary condition (A.8) is no longer needed as there is no melt phase. Since both $\tilde{\gamma}_{ij}$ and $\tilde{X}_{ij}$ satisfy Laplace's equation, Green's second identity allows us to rewrite (A.10) as

$$\tilde{C}_{ijkl} = \frac{1}{2V_{\text{cell}}} \int \tilde{X}_{ij} \frac{\partial \tilde{\gamma}_{kl}}{\partial n} \, \mathrm{d}S. \tag{A.18}$$

For a pure solid, the boundary condition (A.9) applies to the whole boundary of the grain. Substituting (A.9) into (A.18) yields

$$\tilde{C}_{ijkl} = \frac{1}{2V_{\text{cell}}} \int x_p n_p \tilde{X}_{ij} \tilde{N}_{kl} \, \mathrm{d}S, \tag{A.19}$$

511 where $\tilde{N}_{kl}$ and $\tilde{X}_{ij}$ are given by (A.11) and (A.12). The above expression is a key re-
512 sult, as it enables one to calculate the viscosity tensor for Nabarro-Herring creep for a
513 pure solid without explicitly solving Laplace's equation: all one needs to do is evaluate
514 the geometric integral in (A.19).

A.2.1 Isotropic examples

If the fourth rank tensor C_{ijkl} is isotropic, then the result in (A.19) can be written in terms of a shear viscosity as

$$\eta = \frac{1}{2(N+2)(N-1)V_{\text{cell}}} \int \left((\mathbf{x}\cdot\mathbf{n})^2 - \frac{1}{N}(\mathbf{x}\cdot\mathbf{x}) \right) \mathbf{x}\cdot\mathbf{n}\, \mathrm{d}S. \tag{A.20}$$

As a simple example of the use of this formula, consider the unit sphere embedded in N dimensional space ($N = 3$ corresponds to an ordinary sphere, $N = 2$ corresponds to a circle). In this case $\mathbf{x} = \mathbf{n}$ on the surface of the sphere, and $\mathbf{x}\cdot\mathbf{x} = 1$. The integral reduces to

$$\eta = \frac{S}{2V_{\text{cell}}N(N+2)}, \tag{A.21}$$

where S is the surface area. S/V_{cell} for the unit sphere is N, and hence

$$\eta = \frac{1}{2(N+2)}. \tag{A.22}$$

For an ordinary sphere ($N = 3$), $\eta = 1/10$, which is Herring (1950)'s classic result. The corresponding result for a circle ($N = 2$) is $\eta = 1/8$. The formula in (A.20) can be used to directly obtain the shear viscosity for any grain geometry that leads to an isotropic viscosity tensor, including the case of hexagonal grains.

A.2.2 An anisotropic example: orthorhombic grains

For geometries where the viscosity tensor is anisotropic (such as tetrakaidecahedrons), the expression in (A.19) should be used to calculate the viscosity tensor. As an example, consider an orthorhombic grain (a cuboid), with side lengths A_1, A_2, and A_3. The fourth rank tensor $\tilde{C}_{ijkl}$ has orthotropic symmetry. The integrals in (A.19) yield

$$\tilde{C}_{1111} = \frac{1}{108}\left(4A_1^2 + A_2^2 + A_3^2\right), \tag{A.23}$$

$$\tilde{C}_{1122} = \frac{1}{108}\left(-2A_1^2 - 2A_2^2 + A_3^2\right), \tag{A.24}$$

$$\tilde{C}_{1212} = 0, \tag{A.25}$$

where the remaining components of $\tilde{C}_{ijkl}$ can be found by appropriate relabelling of indices and the orthotropic symmetry. The above results agree with those found previously by Lifshitz (1963) and Greenwood (1985), but were determined without explicitly solving Laplace's equation. An important special case of the orthorhombic grain is the unit cube, which has $A_1 = A_2 = A_3 = 1$. As in (40), the tensor $\tilde{C}_{ijkl}$ with cubic symme-

try can then be written in terms of two shear viscosities, given by

$$\eta_1 = \frac{1}{24}, \qquad \eta_2 = 0. \tag{A.26}$$

As discussed by Lifshitz (1963), the vanishing of η_2 arises from a degeneracy in the assumed packing of grains, which allows the array of grains to be freely sheared in some directions without the need for diffusive transport of matter. Note that Greenwood (1992) argues for a non-zero η_2 for cubic grains, but this is based on an erroneous assumption that no minima in the creep strength occurs for principal axes of shear between those parallel to the principal axes of the orthorhombic grain. The packing of tetrakaidecahedral grains considered here has no such degeneracy, and both η_1 and η_2 are non-zero.

A.3 Asymptotics for small porosity and hexagonal grains

A.3.1 Bulk viscosity

For the case of hexagonal grains, it is possible to make further analytical progress when the porosity is non-zero, but small. This can be done through matched asymptotics, and the analysis presented here closely follows a related analysis for the Poisson equation by Ward and Kropinski (2010).

To determine an asymptotic expansion for bulk viscosity, we need to analyse (A.3), (A.4), (A.5) and (A.16) in the limit of infinitesimally small pores (vanishing porosity). The problem can be divided into two parts: First, an outer problem which gives a description at the grain scale, where the pores can be treated as point sources/ point sinks at the vertices of the hexagon. Second, an inner problem, which zooms in on the pore scale behaviour. A matching procedure then joins the two problems in an asymptotically consistent manner.

Dimensionless units are chosen so that the distance between opposite sides of the hexagon is 1. This leads to an area $V_{\text{cell}} = \sqrt{3}/2$, perimeter $S = 2\sqrt{3}$, side length $a = 1/\sqrt{3}$, and perpendicular distance $\mathbf{x} \cdot \mathbf{n} = 1/2$ around the edges of the hexagon. The outer problem can be stated as

$$\nabla^2 \psi = \sum_{k=1}^{6} q\, \delta\left(\mathbf{x} - \mathbf{x}^{(k)}\right) \text{ in } V_{\text{hex}}, \tag{A.27}$$

$$\frac{\partial \psi}{\partial n} = \frac{1}{2} \text{ on } S_{\text{hex}}, \tag{A.28}$$

$$\zeta \sim \frac{1}{4\sqrt{3}} \int \psi \, \mathrm{d}S. \tag{A.29}$$

(A.27) is the equivalent of (A.3), except that point sources have been introduced at the vertices of the hexagon to represent the infinitesimally small pores. Each source has strength q (to be determined), and the vector $\mathbf{x}^{(k)}$ gives the position vector of the k^{th} vertex of the hexagon ($k = 1, 2, \ldots, 6$). (A.28) follows directly from (A.5), and (A.29) follows directly from (A.16).

q can be determined from a balance of flux. The total flux out of the sides of the hexagon is given by integrating (A.28) over the boundary. This flux must be matched by the flux produced by the point sources at the vertices, and hence $q = \sqrt{3}/2$. Since the outer problem involves only Neumann boundary conditions, its solution is unique only up to a constant. This constant will be determined by an appropriate matching to the inner problem, by considering the asymptotic behaviour in the neighbourhood of the point sources. This asymptotic behavior is given for the outer problem by

$$\psi(\mathbf{x}^{(k)}) \sim \frac{q}{2\pi} \log \left| \mathbf{x} - \mathbf{x}^{(k)} \right| + qr \tag{A.30}$$

where the constant r will be determined by matching to the inner solution. The problem in (A.27-A.29) can be solved numerically to yield

$$\zeta \sim \frac{qr}{2} + B \tag{A.31}$$

where the numerical constant $B = -0.177431$.

The inner problem arises from a rescaling of the governing equations. Near $\mathbf{x} = \mathbf{x}^{(k)}$ we introduce the inner variable

$$\mathbf{y} = \frac{\mathbf{x} - \mathbf{x}^{(k)}}{\epsilon} \tag{A.32}$$

where the length scale ϵ is chosen such that the area of an individual pore is π in the inner co-ordinates. For a dihedral angle of 180°, ϵ is equal to the radius of the circular pore. The length scale ϵ is related to the porosity by

$$\epsilon = \left(\frac{\sqrt{3}\phi}{4\pi} \right)^{1/2}. \tag{A.33}$$

The inner problem is

$$\nabla_{\mathbf{y}}^2 \varphi = 0 \text{ in } V, \tag{A.34}$$

$$\varphi = 0 \text{ on } S_{\text{sl}}, \tag{A.35}$$

$$\varphi \sim \alpha \log |\mathbf{y}|, \quad \text{as } |\mathbf{y}| \to \infty. \tag{A.36}$$

(A.34) follows from (A.3), and (A.35) from (A.4). We seek solutions that have a logarithmic singularity in the far-field (A.36) in order to match with the outer solution. The unique solution of inner problem has the following far-field asymptotic behaviour:

$$\varphi \sim \alpha \log |\mathbf{y}| - \alpha \log \kappa(\theta) + \cdots \quad \text{as } |\mathbf{y}| \to \infty \tag{A.37}$$

where $\kappa(\theta)$ is known as the logarithmic capacity. The logarithmic capacity is a function of the shape of the pore, and hence here is a function of the dihedral angle θ (Figure 3).

Matching inner (A.37) and outer (A.30) solutions implies that $\alpha = q/(2\pi)$ and

$$r = -\frac{1}{2\pi} \log \epsilon\kappa(\theta). \tag{A.38}$$

Substituting (A.38) into (A.31) yields the small ϵ asymptotic behaviour of the bulk viscosity,

$$\zeta \sim -\frac{\sqrt{3}}{8\pi} \log \epsilon\kappa(\theta) - 0.177431. \tag{A.39}$$

Using the relationship (A.33) between ϵ and porosity ϕ, (A.39) can also be rewritten in terms of porosity as

$$\zeta \sim -\frac{\sqrt{3}}{16\pi} \log \phi - 0.109145 - \frac{\sqrt{3}}{8\pi} \log \kappa(\theta). \tag{A.40}$$

A.3.2 Shear viscosity

A similar matched asymptotic analysis as performed above for the bulk viscosity can be performed for the shear viscosity. A key difference in the analysis is that while the bulk viscosity is singular as the porosity vanishes, the shear viscosity is finite. Indeed the shear viscosity in the absence of melt can be obtained directly from the integral expression (A.20) to give a value without melt of $\eta_0 = 1/36$. In this section we obtain the next term in the asymptotic expansion, for a small, but finite, amount of melt.

The analysis proceeds as in the previous section by dividing the problem up into two parts: an outer problem for a tensor $\tilde{\psi}_{ij}$ and and inner problem for a tensor $\tilde{\varphi}_{ij}$. Furthermore, it is helpful to subdivide the outer problem as $\tilde{\psi}_{ij} = \tilde{W}_{ij} + \tilde{S}_{ij}$, where $\tilde{W}_{ij}$ is the solution for a pure solid, and $\tilde{S}_{ij}$ is the singular perturbation due to the melt pores. Similarly, the shear viscosity can be subdivided as $\eta = \eta_0 + \eta_S$, where η_S represents the singular perturbation to the shear viscosity.

The problem for the pure solid is

$$\nabla^2 \tilde{W}_{ij} = 0 \text{ in } V_{\text{hex}}, \tag{A.41}$$

$$\frac{\partial \tilde{W}_{ij}}{\partial n} = x_p n_p \tilde{N}_{ij} \text{ on } S_{\text{hex}}, \tag{A.42}$$

where (A.41) follows from (A.7), and (A.42) follows from (A.9). As mentioned above, to determine η_0 is not necessary to solve for $\tilde{W}_{ij}$, but for the asymptotics that follows it is necessary to determine the values of $\tilde{W}_{ij}$ at the vertices of the hexagon. The values at the k^{th} vertex $\mathbf{x}^{(k)}$ can be obtained numerically as

$$\tilde{W}_{ij}\left(\mathbf{x}^{(k)}\right) = F\tilde{X}_{ij}^{(k)} \tag{A.43}$$

where

$$\tilde{X}_{ij}^{(k)} \equiv x_i^{(k)} x_j^{(k)} - x_p^{(k)} x_p^{(k)} \frac{\delta_{ij}}{N} \tag{A.44}$$

and the numerical constant $F = 0.319889078$.

The singular part of the outer problem is

$$\nabla^2 \tilde{S}_{ij} = \sum_{k=1}^{6} q\tilde{X}_{ij}^{(k)}\, \delta\left(\mathbf{x} - \mathbf{x}^{(k)}\right) \text{ in } V_{\text{hex}}, \tag{A.45}$$

$$\frac{\partial \tilde{S}_{ij}}{\partial n} = 0 \text{ on } S_{\text{hex}}, \tag{A.46}$$

$$\eta_S = \frac{1}{4\sqrt{3}} \int \tilde{S}_{kl} \frac{\partial \tilde{X}_{kl}}{\partial n}\, \mathrm{d}S. \tag{A.47}$$

Similar to the bulk viscosity problem, (A.45) is simply (A.7) with the addition of a series of point sources of strength $q\tilde{X}_{ij}^{(k)}$ at the vertices of the hexagon. The choice of tensorial form $\tilde{X}_{ij}^{(k)}$ is motivated by solution of the regular part of the problem at the vertices. (A.46) follows from (A.9), and (A.47) from (A.17). Unlike the outer problem for the bulk viscosity, the problem for $\tilde{S}_{ij}$ is unique if q is given, since the tensor must have zero trace ($\tilde{S}_{kk} = 0$). But in this case, the prefactor q must be determined by matching to the inner solution.

Green's second identity can be used to simplify (A.47) to

$$\eta_S = -\frac{q}{12\sqrt{3}} \sum_{k=1}^{6} \tilde{X}_{kl}\tilde{X}_{kl} = -\frac{q}{36\sqrt{3}}, \tag{A.48}$$

and hence the viscosity can be determined once q is determined. The asymptotic behaviour of $\tilde{S}_{ij}$ near the vertices is

$$\tilde{S}_{ij}(\mathbf{x}^{(k)}) \sim \frac{q\tilde{X}_{ij}^{(k)}}{2\pi} \log\left|\mathbf{x} - \mathbf{x}^{(k)}\right| + qR\tilde{X}_{ij}^{(k)} \tag{A.49}$$

570 where R is determined by numerical computation as $R = 0.150237305$.

The inner problem uses the same scaled variable $\mathbf{y}$ given in (A.32), and is

$$\nabla^2_{\mathbf{y}} \tilde{\varphi}_{ij} = 0 \text{ in } V, \tag{A.50}$$

$$\tilde{\varphi}_{ij} = 0 \text{ on } S_{\text{sl}}, \tag{A.51}$$

$$\tilde{\varphi}_{ij} \sim \alpha \tilde{X}^{(k)}_{ij} \log |\mathbf{y}|, \quad \text{as } |\mathbf{y}| \to \infty. \tag{A.52}$$

The unique solution of inner problem has far-field asymptotic behaviour

$$\tilde{\varphi}_{ij} \sim \alpha \tilde{X}^{(k)}_{ij} \log |\mathbf{y}| - \alpha \tilde{X}^{(k)}_{ij} \log \kappa(\theta) + \cdots \quad \text{as } |\mathbf{y}| \to \infty \tag{A.53}$$

Matching between the inner (A.53) and outer ((A.43) and (A.49)) solutions yields

$$\alpha = \frac{q}{2\pi}, \tag{A.54}$$

$$F + qR = -\alpha \log \epsilon\kappa(\theta), \tag{A.55}$$

and hence

$$q = -\frac{2\pi F}{2\pi R + \log \epsilon\kappa(\theta)}. \tag{A.56}$$

Substituting (A.56) into (A.48) yields the asymptotic expression for the shear viscosity for small ϵ,

$$\eta \sim \frac{1}{36} + \frac{2\pi F}{36\sqrt{3}\,(2\pi R + \log \epsilon\kappa(\theta))}, \tag{A.57}$$

571 where the numerical constants are $F = 0.319889078$ and $R = 0.150237305$.

572 A.4 Leading-order bulk viscosity asymptotics for general grain shapes

Part of the asymptotic analysis given in section A.3.1 for hexagonal grains can be applied in three-dimensions to obtain the leading-order behaviour of the bulk viscosity for more general grain shapes. Instead of the outer problem consisting of point sources of strength q at the vertices of the hexagon, we now consider line sources of strength q along grain edges in 3D. This assumes melt forms a connected network along the grain edges at vanishing porosity, which will only be true for dihedral angles less than 60°. Integration of (A.5) around the surface of the grain gives the net flux out of the grain faces as $Q = NV_{\text{cell}}$. This must match the flux produced by the line sources, $Q = qL$, where L is the total length of edges for the unit cell (an effective length accounting for the fact that each edge is shared by more than one grain). Hence

$$q = \frac{N}{\lambda}, \tag{A.58}$$

where $\lambda \equiv L/V_{\text{cell}}$ is the edge length per unit volume in the tiling of grains. For tetrakaidecahedrons, $\lambda = 6\sqrt{2}$ in units where the distance between opposite square faces of the tetrakaidecahedrons is 1. The equivalent measure for hexagonal grains in 2D is the density of vertices per unit area, where $\lambda = 4/\sqrt{3}$ in units where the distance between opposite sides of the hexagons is 1.

The asymptotic behaviour in the neighbourhood of the line sources in 3D will take the same form as (A.30), with bulk viscosity given in N-dimensions as

$$\zeta \sim \frac{qr}{N} \tag{A.59}$$

to leading order (this is the N-dimensional counterpart to (A.31)). A similar matching to that in (A.38) yields

$$r \sim -\frac{1}{4\pi} \log \phi \tag{A.60}$$

at leading order. Substituting (A.60) into (A.59) gives the leading order asymptotics

$$\zeta \sim -\frac{1}{4\pi\lambda} \log \phi \tag{A.61}$$

where the next term in the asymptotic expansion will depend on the exact geometry of the melt. For the specific case of tetrakaidecahedrons with distance 1 between square faces,

$$\zeta \sim -\frac{1}{24\pi\sqrt{2}} \log \phi. \tag{A.62}$$

A.5 Parametrisation of Nabarro-Herring creep

It is useful to have a simple parametrisation of viscosity as a function of porosity which can be used in larger-scale models. What follows is a suggested parametrisation for Nabarro-Herring creep, which provides a close approximation to the tetrakaidecahedron calculations here for a dihedral angle of 40° (appropriate for basaltic melts) and porosities up to around 10%, where melt exists as a connected network along the grain edges. The formulas below are least-squares polynomial fits in terms of a variable $\nu \equiv -1/\log\phi$, where this choice of variable has been motivated by the asymptotic analysis above. The leading-order term in the fits is provided the leading-order asymptotics for small porosity. The higher-order terms have been found by fitting the numerical results

shown in Figures 5 and 6. The parametrisation is

$$\frac{\eta}{\eta_0} = 1 + a_1\nu + a_2\nu^2 + a_3\nu^3, \tag{A.63}$$

$$\frac{\zeta}{\eta} = \frac{160\sqrt{2}}{139\pi}\frac{1}{\nu} + b_1 + b_2\nu + b_3\nu^2, \tag{A.64}$$

where the fitting constants are

$$a_1 = -4.28207265, \quad a_2 = 7.36988663, \quad a_3 = -4.98396638, \tag{A.65}$$

$$b_1 = 0.97736898, \quad b_2 = -1.76154195, \quad b_3 = 2.63720462. \tag{A.66}$$

B Coble creep analytical solutions

B.1 Pure solid, Hexagonal grains

Simple analytical solutions exist for Coble creep in arrays of regular hexagons (Cocks & Searle, 1990; Spingarn & Nix, 1978). The Poisson equation for the tensor $\underline{\underline{\gamma}}$ in (32) can be written in co-ordinates along a single edge of the hexagon as

$$-\nabla_\perp^2 \underline{\underline{\gamma}} = \begin{pmatrix} 0 & 0 \\ 0 & 1 \end{pmatrix} \tag{B.1}$$

where the horizontal co-ordinate is along an edge and the vertical coordinate is perpendicular to the edge (i.e. the normal vector is $\mathbf{n} = (0, 1)$). Since the edge is straight the surface Laplacian operator $\nabla_\perp^2$ becomes $\mathrm{d}^2/\mathrm{d}s^2$ where s measures distance along an edge. s is chosen to be zero in the middle of an edge, and equal to h at one end and $-h$ at the other end. In the absence of melt $h = 1/(2\sqrt{3})$ with lengths scaled such that the distance between opposite sides of the hexagon is 1. (B.1) can be integrated as

$$\underline{\underline{\gamma}} = \begin{pmatrix} a_{11} + b_{11}s & a_{12} + b_{12}s \\ a_{12} + b_{12}s & a_{22} + b_{22}s - \frac{1}{2}s^2 \end{pmatrix} \tag{B.2}$$

for constants a_{ij} and b_{ij} that will be determined by the boundary conditions.

(B.2) can be simplified immediately by the mirror symmetry of the hexagon along a plane through the middle of an edge, which yields

$$\underline{\underline{\gamma}} = \begin{pmatrix} a_{11} & b_{12}s \\ b_{12}s & a_{22} - \frac{1}{2}s^2 \end{pmatrix}. \tag{B.3}$$

By the rotational symmetry of the hexagon, the solution for $\underline{\underline{\gamma}}$ on the other 5 edges is the same, up to a suitable rotation of the coordinates. Thus in what follows we find the solution just for one edge of the hexagon, exploiting the symmetry to match this solution to the solutions on the other edges.

586 ### *B.1.1 Isolated grain*

In the absence of melt, what the effective viscosity is depends very much on the nature of the assumed boundary conditions. Since there is no melt present, the medium is incompressible, and this restricts the discussion to the trace-free part of $\underline{\underline{\gamma}}$, which is denoted as $\underline{\underline{\tilde{\gamma}}}$. Following on from (B.3), this can be written in terms of just two constants, a and b,

$$\underline{\underline{\tilde{\gamma}}} = \begin{pmatrix} -a + \frac{1}{4}s^2 & bs \\ bs & a - \frac{1}{4}s^2 \end{pmatrix} \tag{B.4}$$

where the constants will be determined by the choice of boundary condition. Given the rotational symmetry of the hexagon, it is helpful to describe the boundary conditions using the rotation matrix

$$\underline{\underline{\boldsymbol{R}}}_{\theta} = \begin{pmatrix} \cos\theta & -\sin\theta \\ \sin\theta & \cos\theta \end{pmatrix}. \tag{B.5}$$

If one considers each individual grain to be isolated, and grain-boundary diffusion to be restricted to each individual grain (as Takei and Holtzman (2009a) do), then at each corner of the grain we must have continuity of vacancies (chemical potential) and continuity of flux. Continuity of vacancies can be written as

$$\underline{\underline{\tilde{\gamma}}}(s = h) = \underline{\underline{\boldsymbol{R}}}_{-\pi/3} \cdot \underline{\underline{\tilde{\gamma}}}(s = -h) \cdot \underline{\underline{\boldsymbol{R}}}^T_{-\pi/3} \tag{B.6}$$

which simply ensures that the concentration at the end of one edge matches the start of the next. By symmetry the solution on one edge is related to the solution on another edge simply by a rotation of co-ordinates. Continuity of flux is

$$\frac{\mathrm{d}\underline{\underline{\tilde{\gamma}}}}{\mathrm{d}s}(s = h) = \underline{\underline{\boldsymbol{R}}}_{-\pi/3} \cdot \frac{\mathrm{d}\underline{\underline{\tilde{\gamma}}}}{\mathrm{d}s}(s = -h) \cdot \underline{\underline{\boldsymbol{R}}}^T_{-\pi/3}, \tag{B.7}$$

since the flux is given by the derivative of concentration along each edge. (B.6) and (B.7) determine the constants in (B.4) as

$$a = \frac{5}{144}, \qquad b = \frac{1}{12}. \tag{B.8}$$

587 ### *B.1.2 Networked*

Alternatively, if the grain boundaries form a connected network along which diffusion can occur, then the boundary conditions are slightly different. Continuity of vacancies is unchanged and given by (B.6), but continuity of flux becomes

$$\frac{\mathrm{d}\underline{\underline{\tilde{\gamma}}}}{\mathrm{d}s}(s = h) = \underline{\underline{\boldsymbol{R}}}_{-\pi/3} \cdot \frac{\mathrm{d}\underline{\underline{\tilde{\gamma}}}}{\mathrm{d}s}(s = -h) \cdot \underline{\underline{\boldsymbol{R}}}^T_{-\pi/3} + \underline{\underline{\boldsymbol{R}}}_{\pi/3} \cdot \frac{\mathrm{d}\underline{\underline{\tilde{\gamma}}}}{\mathrm{d}s}(s = -h) \cdot \underline{\underline{\boldsymbol{R}}}^T_{\pi/3} \tag{B.9}$$

because the flux balance is now between the three edges that meet at each triple junction (Figure 7). (B.6) and (B.9) determine the constants in (B.4) as

$$a = \frac{1}{48}, \qquad b = 0. \tag{B.10}$$

Once $\underline{\underline{\tilde{\gamma}}}$ is determined it is straightforward to integrate (35) to find the relevant viscosities. For the matrix given in (B.4), the shear viscosity is

$$\eta = \frac{a}{2} + \frac{b}{36} - \frac{1}{288}, \tag{B.11}$$

and hence $\eta = 7/432$ for a pure solid under the isolated assumption and $\eta = 1/144$ for a pure solid under the networked assumption.

B.2 Coble creep with melt

In the presence of melt, the equations of Coble creep can be further simplified. The solution to (32) can be broken down into a series of isolated Poisson problems on each individual grain–grain contact. Moreover, since we are assuming the boundaries are planar, we can write these individual Poisson problems in terms of a single scalar variable φ, since the normal vector $\mathbf{n}$ is a constant over each grain–grain contact. Writing $\gamma_{ij} = \varphi n_i n_j$, (32) and (35) become

$$-\nabla_\perp^2 \varphi = 2 x_p n_p, \tag{B.12}$$

$$C_{ijkl} = \frac{1}{V_{\text{cell}}} \int \varphi x_i n_j n_k n_l \, \mathrm{d}S. \tag{B.13}$$

The tensor C_{ijkl} satisfies the following symmetry, known as the Cauchy relation,

$$C_{ijkl} = C_{ikjl}. \tag{B.14}$$

As a consequence of the above symmetry, for isotropic cases the following relationship holds between the bulk and shear viscosities,

$$\frac{\zeta}{\eta} = \frac{N+2}{N}, \tag{B.15}$$

so $\zeta = 2\eta$ in 2D, and $\zeta = \frac{5}{3}\eta$ in 3D.

The integral in (B.13) can be further simplified by considering the integral as a sum over the contributions from each grain–grain contact,

$$C_{ijkl} = \frac{1}{V_{\text{cell}}} \sum_f n_i^f n_j^f n_k^f n_l^f d_f \int \varphi \, \mathrm{d}S, \tag{B.16}$$

where f is an index used to denote the individual grain–grain contacts, and $\mathbf{n}^f$ are the corresponding normals to those contacts. d_f are the perpendicular distances of the contacts from the origin. (B.16) has been obtained from (B.13) by pulling out the $n_j n_k n_l$ factor in front of the integral sign, which can be done because $\mathbf{n}$ is constant on each contact. What remains in the integrand of (B.13) is then φx_i, which yields a vector quantity for the integral. However, provided the contact face has at least one non-trivial symmetry (e.g. symmetric under reflection or rotation), this vector quantity must be proportional to the normal vector, and hence a factor of n_i can also be pulled in front of the integral to yield the final scalar integral expression in (B.16).

The right hand side of (B.12) is constant over each contact, equal to twice the perpendicular distance from the origin. Hence the procedure for calculating C_{ijkl} consists of solving a series of Poisson problems with constant right-hand side for each face, and then integrating the resulting solution over the contact. This is identical to the problem of finding the hydraulic resistance in Hagen-Poiseuille flow in a pipe of given cross-sectional shape (Bazant, 2016; Mortensen, Okkels, & Bruus, 2005). The hydraulic resistance depends both on the cross-sectional area and the particular cross-sectional shape of the pipe. The same is true here of the effective viscosity tensor for Coble creep, which depends both on the areas of the contact patches and their shapes. The two effects can be separated by introducing the following scaled problem on each contact face,

$$-\nabla_\perp^2 w_f = 1, \tag{B.17}$$

$$\chi_f = \frac{1}{A_f^{(N+1)/(N-1)}} \int w_f \, \mathrm{d}S, \tag{B.18}$$

where χ_f is a shape factor, defined such that it is independent of the area of the contact. On each contact $\varphi = 2 d_f w_f$. The viscosity tensor can then be written

$$C_{ijkl} = \frac{2}{V_{\text{cell}}} \sum_f n_i^f n_j^f n_k^f n_l^f d_f^2 \chi_f A_f^{(N+1)/(N-1)}. \tag{B.19}$$

For the tetrakaidecahedral geometry considered here the contact faces go from being squares and hexagons at zero porosity, to being more circular at higher porosity. For a circle $\chi = 1/(8\pi) = 0.0397887$, for a hexagon $\chi = 0.0383503$, and for a square $\chi = 0.0351443$. χ is very similar for all three end-member shapes, so the shape effects on the viscosity are likely to be modest. The principal control on the viscosity tensor is contact area. In 3D, the viscosity is proportional to A_f^2 and in 2D, the viscosity is proportional to A_f^3. This agrees with the results of Cooper and Kohlstedt (1984) and Takei and Holtzman (2009a),

608 and indeed, (B.19) is a generalisation of (42) of Takei and Holtzman (2009a) to a more
609 general geometry.

The bulk viscosity can be obtained from (B.19) as

$$\zeta = \frac{2}{N^2 V_{\text{cell}}} \sum_f d_f^2 \chi_f A_f^{(N+1)/(N-1)}. \tag{B.20}$$

610 ***B.2.1 Hexagonal grains***

For the hexagon in 2D, $N = 2$, $V_{\text{cell}} = \sqrt{3}/2$, $d_f = 1/2$, $\chi_f = 1/12$, and $A_f = \rho/\sqrt{3}$, where $\rho \equiv A_{\text{ss}}/A_{\text{cell}}$ is the fraction of the unit cell boundary which is grain–grain contact. The bulk viscosity is given by (B.20) as $\zeta = \rho^3/72$, in agreement with Cocks and Searle (1990). From (B.15), the shear viscosity $\eta = \zeta/2 = \rho^3/144$. Some straightforward trigonometry can be used to relate ρ to θ and ϕ by

$$\phi = (1-\rho)^2 \phi_d(\theta) \tag{B.21}$$

where

$$\phi_d(\theta) = \frac{1}{8\sqrt{3}} \csc\left(\tfrac{\pi}{6} - \tfrac{\theta}{2}\right) \left(4\sqrt{3}\cos\tfrac{\theta}{2} - (\pi - 3\theta)\csc\left(\tfrac{\pi}{6} - \tfrac{\theta}{2}\right)\right). \tag{B.22}$$

611 ***B.2.2 Tetrakaidecahedral grains***

For tetrakaidecahedrons, (B.19) can be simplified to give the two shear viscosities as

$$\eta_1 = \frac{1}{3V_{\text{cell}}} \sum_{\text{squares}} d_f^2 \chi_f A_f^2, \tag{B.23}$$

$$\eta_2 = \frac{2}{9V_{\text{cell}}} \sum_{\text{hexagons}} d_f^2 \chi_f A_f^2, \tag{B.24}$$

where η_1 is given in terms of a sum over the square faces only, and η_2 is terms of a sum over the hexagonal faces only. The bulk viscosity is given by $\zeta = \frac{5}{3}\overline{\eta} = \frac{2}{3}\eta_1 + \eta_2$. In coordinates where the distance between opposite square faces is 1, $V_{\text{cell}} = 1/2$, $d_{\text{sq}} = 1/2$, and $d_{\text{hex}} = \sqrt{3}/4$. When there is only an infinitesimal amount of melt present, $A_{\text{sq}} = 1/8$ and $A_{\text{hex}} = 3\sqrt{3}/16$, and hence

$$\eta_{10} = \frac{\chi_{\text{sq}}}{64}, \tag{B.25}$$

$$\eta_{20} = \frac{9\chi_{\text{hex}}}{128}, \tag{B.26}$$

612 and these are the values given in the shorted row of Table 1.

References

Alisic, L., Rhebergen, S., Rudge, J. F., Katz, R. F., & Wells, G. N. (2016). Torsion of a cylinder of partially molten rock with a spherical inclusion: Theory and simulation. *Geochemistry, Geophys. Geosystems*, *17*(1), 143–161. doi: 10.1002/2015GC006061

Arzt, E., Ashby, M. F., & Easterling, K. E. (1983). Practical Applications of Hotlsostatic Pressing Diagrams : Four Case Studies. *Metall. Trans. A*, *14A*, 211–221. doi: 10.1007/BF02651618

Bazant, M. Z. (2016). Exact solutions and physical analogies for unidirectional flows. *Phys. Rev. Fluids*, *1*(2), 024001. doi: 10.1103/PhysRevFluids.1.024001

Beeré, W. (1976). Stress redistribution during Nabarro-Herring and superplastic creep. *Met. Sci.*, *10*(4), 133–139. doi: doi:10.1179/030634576790431958

Bercovici, D., Ricard, Y., & Schubert, G. (2001). A two-phase model for compaction and damage 1. General theory. *J. Geophys. Res.*, *106*(B5), 8887–8906. doi: 10.1029/2000JB900430

Bercovici, D., & Rudge, J. F. (2016). A mechanism for mode selection in melt band instabilities. *Earth Planet. Sci. Lett.*, *433*, 139–145. doi: 10.1016/j.epsl.2015.10.051

Coble, R. L. (1963). A Model for Boundary Diffusion Controlled Creep in Polycrystalline Materials. *J. Appl. Phys.*, *34*(6), 1679–1682. doi: 10.1063/1.1702656

Cocks, A. C. F. (1996). Variational principles, numerical schemes and bounding theorems for deformation by Nabarro-Herring creep. *J. Mech. Phys. Solids*, *44*(9), 1429–1452. doi: 10.1016/0022-5096(96)00040-3

Cocks, A. C. F., & Searle, A. A. (1990). Cavity growth in ceramic materials under multiaxial stress states. *Acta Metall. Mater.*, *38*(12), 2493–2505. doi: 10.1016/0956-7151(90)90261-E

Cooper, R. F. (1990). Differential stress-induced melt migration: An experimental approach. *J. Geophys. Res.*, *95*(B5), 6979. doi: 10.1029/JB095iB05p06979

Cooper, R. F., & Kohlstedt, D. L. (1984). Solution-precipitation enhanced diffusional creep of partially molten olivine-basalt aggregates during hot-pressing. *Tectonophysics*, *107*(3-4), 207–233. doi: 10.1016/0040-1951(84)90252-X

Cooper, R. F., & Kohlstedt, D. L. (1986). Rheology and structure of olivine-basalt partial melts. *J. Geophys. Res.*, *91*(B9), 9315. doi: 10.1029/JB091iB09p09315

Cooper, R. F., Kohlstedt, D. L., & Chyung, K. (1989). Solution-precipitation enhanced creep in solid-liquid aggregates which display a non-zero dihedral angle. *Acta Metall.*, *37*(7), 1759–1771. doi: 10.1016/0001-6160(89)90061-8

Driscoll, T. A. (2002). *Schwarz-Christoffel Toolbox User's Guide, Version 2.3.* Retrieved from `http://www.math.udel.edu/{~}driscoll/SC/`

Driscoll, T. A., & Trefethen, L. N. (2002). *Schwarz-Christoffel Mapping.* Cambridge University Press.

Faul, U. H., & Jackson, I. (2007). Diffusion creep of dry, melt-free olivine. *J. Geophys. Res. Solid Earth*, *112*(B4), 1–14. doi: 10.1029/2006JB004586

Ford, J. M., & Wheeler, J. (2004). Modelling interface diffusion creep in two-phase materials. *Acta Mater.*, *52*(8), 2365–2376. doi: 10.1016/j.actamat.2004.01.045

German, R. M., Suri, P., & Park, S. J. (2009). Review: Liquid phase sintering. *J. Mater. Sci.*, *44*(1), 1–39. doi: 10.1007/s10853-008-3008-0

Greenwood, G. W. (1985). An analysis of the effect of multiaxial stresses and grain shape on Nabarro-Herring creep. *Philos. Mag. A*, *51*(4), 537–542. doi: 10.1080/01418618508237575

Greenwood, G. W. (1992). A Formulation for Anisotropy in Diffusional Creep. *Proc. R. Soc. A Math. Phys. Eng. Sci.*, *436*(1896), 187–196. doi: 10.1098/rspa.1992.0013

Herring, C. (1950). Diffusional Viscosity of a Polycrystalline Solid. *J. Appl. Phys.*, *21*(5), 437–445. doi: 10.1063/1.1699681

Hewitt, I. J., & Fowler, A. C. (2008). Partial melting in an upwelling mantle column. *Proc. Roy. Soc. A*, *464*(2097), 2467–2491. doi: 10.1098/rspa.2008.0045

Holtzman, B. K. (2016). Questions on the existence, persistence, and mechanical effects of a very small melt fraction in the asthenosphere. *Geochemistry, Geophys. Geosystems*, *17*(2), 470–484. doi: 10.1002/2015GC006102

Holtzman, B. K., Groebner, N. J., Zimmerman, M. E., Ginsberg, S. B., & Kohlstedt, D. L. (2003). Stress-driven melt segregation in partially molten rocks. *Geochemistry, Geophys. Geosystems*, *4*(5), 8607. doi: 10.1029/2001GC000258

Katz, R. F., Spiegelman, M., & Holtzman, B. (2006). The dynamics of melt and shear localization in partially molten aggregates. *Nature*, *442*(7103), 676–679. doi: 10.1038/nature05039

Lifshitz, I. M. (1963). On the theory of diffusion-viscous flow of polycrystalline bod-

ies. *Sov. Phys. JETP*, *17*(44), 1349–1367.

Logg, A., Mardal, K.-A., & Wells, G. (Eds.). (2012). *Automated Solution of Differential Equations by the Finite Element Method, Lecture Notes in Computational Science and Engineering.* vol 84, Springer, Berlin Heidelberg.

Logg, A., & Wells, G. N. (2010). DOLFIN. *ACM Trans. Math. Softw.*, *37*(2), 1–28. doi: 10.1145/1731022.1731030

McCarthy, C., & Takei, Y. (2011). Anelasticity and viscosity of partially molten rock analogue: Toward seismic detection of small quantities of melt. *Geophys. Res. Lett.*, *38*(18), L18306. doi: 10.1029/2011GL048776

McKenzie, D. (1984). The Generation and Compaction of Partially Molten Rock. *J. Pet.*, *25*, 713–765. doi: 10.1093/petrology/25.3.713

Mei, S., Bai, W., Hiraga, T., & Kohlstedt, D. L. (2002). Influence of melt on the creep behavior of olivine-basalt aggregates under hydrous conditions. *Earth Planet. Sci. Lett.*, *201*(3-4), 491–507. doi: 10.1016/S0012-821X(02)00745-8

Mortensen, N. A., Okkels, F., & Bruus, H. (2005). Reexamination of Hagen-Poiseuille flow: Shape dependence of the hydraulic resistance in microchannels. *Phys. Rev. E*, *71*(5), 057301. doi: 10.1103/PhysRevE.71.057301

Nabarro, F. R. N. (1948). Deformation of crystals by the motion of single ions. In *Report on conf. on the strength of solids* (pp. 75–90). Physical Society, London.

Pan, J., & Cocks, A. (1994). A constitutive model for stage 2 sintering of fine grained materials—I. Grain-boundaries act as perfect sources and sinks for vacancies. *Acta Metall. Mater.*, *42*(4), 1215–1222. doi: 10.1016/0956-7151(94)90138-4

Qi, C., Zhao, Y.-H., & Kohlstedt, D. L. (2013). An experimental study of pressure shadows in partially molten rocks. *Earth Planet. Sci. Lett.*, *382*, 77–84. doi: 10.1016/J.EPSL.2013.09.004

Raj, R., & Ashby, M. F. (1971). On grain boundary sliding and diffusional creep. *Metall. Trans.*, *2*(4), 1113–1127. doi: 10.1007/BF02664244

Rees Jones, D. W., & Katz, R. F. (2018). Reaction-infiltration instability in a compacting porous medium. *J. Fluid Mech.*, *852*, 5–36. doi: 10.1017/jfm.2018.524

Rudge, J. F. (2018). Textural equilibrium melt geometries around tetrakaidecahe-

dral grains. *Proc. R. Soc. A Math. Phys. Eng. Sci.*, *474*(2212), 20170639. doi: 10.1098/rspa.2017.0639

Rudge, J. F., & Bercovici, D. (2015). Melt-band instabilities with two-phase damage. *Geophys. J. Int.*, *201*(2), 640–651. doi: 10.1093/gji/ggv040

Schmeling, H., Kruse, J. P., & Richard, G. (2012). Effective shear and bulk viscosity of partially molten rock based on elastic moduli theory of a fluid filled poroelastic medium. *Geophys. J. Int.*, *190*(3), 1571–1578. doi: 10.1111/j.1365-246X.2012.05596.x

Scott, D. R., & Stevenson, D. J. (1986). Magma ascent by porous flow. *J. Geophys. Res.*, *91*(B9), 9283–9296. doi: 10.1029/JB091iB09p09283

Shah, S., & Chokshi, A. H. (1998). The significance of diffusional flow in ultrafine-grained materials. *Colloids Surfaces A Physicochem. Eng. Asp.*, *133*(1-2), 57–61. doi: 10.1016/S0927-7757(97)00124-6

Simpson, G., Spiegelman, M., & Weinstein, M. I. (2010). A multiscale model of partial melts: 2. Numerical results. *J. Geophys. Res.*, *115*(B4), B04411. doi: 10.1029/2009JB006376

Sleep, N. H. (1988). Tapping of melt by veins and dikes. *J. Geophys. Res. Solid Earth*, *93*(B9), 10255–10272. doi: 10.1029/JB093iB09p10255

Spiegelman, M. (2003). Linear analysis of melt band formation by simple shear. *Geochemistry, Geophys. Geosystems*, *4*(9), 8615. doi: 10.1029/2002GC000499

Spingarn, J. R., & Nix, W. D. (1978). Diffusional creep and diffusionally accommodated grain rearrangement. *Acta Metall.*, *26*(9), 1389–1398. doi: 10.1016/0001-6160(78)90154-2

Stevenson, D. J. (1989). Spontaneous small-scale melt segregation in partial melts undergoing deformation. *Geophys. Res. Lett.*, *16*(9), 1067–1070. doi: 10.1029/GL016i009p01067

Takei, Y., & Holtzman, B. K. (2009a). Viscous constitutive relations of solid-liquid composites in terms of grain boundary contiguity: 1. Grain boundary diffusion control model. *J. Geophys. Res. Solid Earth*, *114*(6), 1–19. doi: 10.1029/2008JB005850

Takei, Y., & Holtzman, B. K. (2009b). Viscous constitutive relations of solid-liquid composites in terms of grain boundary contiguity: 2. Compositional model for small melt fractions. *J. Geophys. Res.*, *114*(B6), B06206. doi:

10.1029/2008JB005851

Takei, Y., & Katz, R. F. (2015). Consequences of viscous anisotropy in a deforming, two-phase aggregate. Why is porosity-band angle lowered by viscous anisotropy? *J. Fluid Mech.*, *784*, 199–224. doi: 10.1017/jfm.2015.592

von Bargen, N., & Waff, H. S. (1986). Permeabilities, interfacial-areas and curvatures of partially molten systems - results of numerical computation of equilibrium microstructures. *J. Geophys. Res.*, *91*, 9261–9276.

Ward, M. J. M., & Kropinski, M.-C. M. (2010). Asymptotic Methods for PDE Problems in Fluid Mechanics and Related Systems with Strong Localized Perturbations in Two-Dimensional Domains. In *Asymptotic methods in fluid mechanics: Survey and recent advances. cism courses and lectures, vol 523* (pp. 1–48). Vienna: Springer, Vienna. doi: 10.1007/978-3-7091-0408-8_2

Yamauchi, H., & Takei, Y. (2016). Polycrystal anelasticity at near-solidus temperatures. *J. Geophys. Res. Solid Earth*, *121*(11), 7790–7820. doi: 10.1002/2016JB013316